Complete citation:

Ahmadi, F., Ebrahimian, M., Sanders, R. S., & Ghaemi, S. (2019). Particle image and tracking velocimetry of solid-liquid turbulence in a horizontal channel flow. International Journal of Multiphase Flow, 112, 83-99. doi: 10.1016/j.ijmultiphaseflow.2018.12.007

The final publication is available at https://doi.org/10.1016/j.ijmultiphaseflow.2018.12.007

Particle image and tracking velocimetry of solid-liquid turbulence in a horizontal channel flow

Farzad Ahmadi[1], Masoud Ebrahimian[1], R. Sean Sanders[2] and Sina Ghaemi[1*]

[1] Department of Mechanical Engineering, University of Alberta, Edmonton, Alberta, Canada, T6G 2G8

[2] Department of Chemical and Materials Engineering, University of Alberta, Edmonton, Alberta, Canada, T6G 2V4

Abstract

The turbulence statistics of the solid and liquid phases in a horizontal turbulent channel flow are experimentally investigated to identify the effect of particle size, flow Reynolds number (*Re*) and the volumetric concentration of particles. Glass beads with diameters of 285, 340, 530 and 700 μm are used to produce suspensions at particle volumetric concentrations between 0.05 to 0.18%. Measurements are made at *Re* of 50,000, 75,000, 100,000, and 125,000 based on channel height and average velocity. The instantaneous velocity of the glass beads is obtained using a correlation-based particle tracking velocimetry (PTV) while particle image velocimetry (PIV) using smaller tracers is applied simultaneously to obtain the liquid phase velocity. It is observed that the solid phase velocity is larger than the liquid phase in the near-wall region for the larger particles and higher flow *Re*. The particle *Re* number, Re_p, defined based on the particle diameter and the slip velocity (mean relative velocity between the liquid and solid phases), and the Stokes number (*St*) are used to evaluate the turbulence modulation of the liquid phase. Particle *Re* numbers as large as 225 are calculated for the 700 μm particles at *Re* = 125,000, which leads to vortex shedding and, consequently, increases turbulence intensity of the liquid phase relative to the unladen flow. The PTV results indicate that the turbulence intensity of the solid phase decreases with increase of *St* (i.e. larger particles and higher flow *Re*). The solid phase volumetric concentration has negligible effect on the solid phase turbulence, while the wall-normal turbulence intensity of the liquid phase increases with the volumetric concentration. This observation reveals the two-way coupling of the solid and liquid phases at the range of concentrations investigated in the current study.

Keywords:

[*] Corresponding author
E-mail address: ghaemi@ualberta.ca (S. Ghaemi).

Particle-laden flow, Turbulence intensity, Turbulence modulation, Particle image velocimetry, Particle tracking velocimetry

1. Introduction

The transportation of mixtures of particles and liquids using slurry pipelines plays a crucial role in the petroleum and mining industries. Slurry pipeline flow is typically turbulent and the presence of the particulate phase results in pipe wear and increased pumping cost (Roco and Addie, 1987; Tsuji et al., 1985; Zisselmar and Molerus, 1979). As a result, slurry pipeline design and operation relies on analysis and modelling of turbulent two-phase flows. This has motivated experimental and numerical investigation of turbulence statistics of the carrier and particulate phases, the interaction between the two phases, and spatial distribution of particles in liquid-solid (and gas-solid) turbulent flows.

Many of the earlier studies focused on gas-solid flows, where the influence of solid particles on the overall flow and on the continuous phase is greater than in liquid-continuous flows because of the larger density ratio and mass loading in gas-solid systems. That said, there are many similarities between particle-laden liquid and gas flows: for example, the addition of particles flattens the mean velocity profile of the carrier phase in the core region of the pipe (Nouri et al., 1987; Tsuji et al., 1984; Tsuji and Morikawa, 1982). In horizontal air-solid channel flows, the maximum velocity moves away from the pipe axis due to the asymmetric distribution of the particles (Tsuji and Morikawa, 1982). In vertical gas-solid flows, Tsuji et al. (1984) observed a concave velocity profile with a local minimum at the center of the pipe (Tsuji et al., 1984). Vreman (2015) observed that the mean velocity profile of the particles in downward air-solid flow is flatter than the velocity profile of the carrier phase in the core region of channel. Nouri et al. (1987) also observed that the velocity difference between the particles and the unladen fluid decreases as the Reynolds number (Re) increases ~~up to 40,000~~ in a descending liquid-solid pipe flow. As this short review reveals, there are many factors that influence the behavior of particle-laden flows. The difference in previous results is due to the wide range of condition. Therefore, for closer relevance to mining and petroleum industry, experiments in high Re horizontal solid-liquid flows is required.

One phenomenon that is particularly poorly understood, and one that most models do not properly address, is the fact that carrier phase turbulence can be attenuated or amplified by the presence of the particles. The change in carrier phase turbulence kinetic energy when particles are added is referred to as turbulence modulation, which depends on several parameters including the flow Re, particle density and size, and volumetric concentration (φ_v) of the solid phase (Gore and Crowe, 1989). The former factors are quantified using the particle Reynolds number (Re_p), which is defined based on the slip velocity and particle diameter. Measurements of Tsuji et al. (1984) in a gas-solid vertical pipe flow showed that 3 mm polystyrene spheres with Re_p = 470 intensifies the carrier phase turbulence. They attributed the turbulence augmentation to vortex shedding based on the large Re_p. Although Re_p is a critical parameter to characterize carrier phase turbulence

modulation, it is difficult to estimate the slip velocity *a priori* since it depends to a great extent on the carrier phase turbulence (Doroodchi et al., 2008) and local particle concentration (Lee, 1987). Tanaka and Eaton (2008) introduced a particle momentum number (*Pa*) to model turbulence modulation in a large set of experimental data. The *Pa* combines Stokes number (*St*) with flow *Re*, Kolmogorov length scale, and the characteristic dimension of the conduit. They observed that particles with $Pa < 10^3$ or $Pa > 10^5$ augment the turbulence kinetic energy while attenuation occurs when $10^3 < Pa < 10^5$. It is important to note that for the set of data examined by Tanaka and Eaton (2008), *Re* was limited to 30,000. The experiments of the current investigation will extend evaluation of turbulence modulation to *Re* higher than 125,000.

There are a limited number of investigations focusing on the turbulent statistics of the dispersed (solid) phase. The effects of particle concentration, particle size and density and flow conditions (e.g. flow *Re*) have been investigated, typically over narrow ranges. As described in the following paragraphs, different investigations sometimes provided conflicting results. Tsuji and Morikawa (1982) measured solid-phase turbulence in a horizontal pipe flow of an air-continuous system using laser Doppler anemometry (LDA). They observed a relatively uniform and flat distribution of solid-phase streamwise turbulence intensity across most of the cross-section, which decreased with increasing particle concentration. Nouri et al. (1987) also used LDA to observe the reduction of streamwise turbulence intensity of acrylic particles in water with the increase of volumetric concentration from 0.1% to 14% in a vertical pipe. The LDA measurements of Kulick et al. (1994) also showed reduction of the turbulence intensity of copper particles in a channel flow of air with increasing particle concentration. The decreasing particle turbulence intensity at higher particle concentrations has been associated with the rise in the number of inelastic particle collisions. Most studies on particulate phase turbulence were carried out in solid-gas flows or in vertical pipes. The influence of volumetric concentration on turbulence in horizontal solid-liquid systems remains unexplored, and is addressed in the current investigation.

Measurements in solid-gas flows have shown that, in general, larger and heavier particles result in higher streamwise particle turbulence intensity. Kussin and Sommerfeld (2002) observed the increase of particle turbulence intensity when the diameter of glass beads increases from 60 to 190 μm in a channel flow of air. They associated the trend with larger particle inertia and more collisions with the wall. Kulick et al. (1994) indicated that the streamwise turbulence intensity of particles also increases with increase of particle density. The effect of particle size on turbulence intensity in an upward liquid flow was investigated by Shokri et al. (2017) using combined PIV and PTV. They investigated 0.5, 1 and 2 mm glass beads at $Re = 320{,}000$ and observed, in contrast to the result of Kussin and Sommerfeld (2002), that the smaller particles have higher near-wall turbulence. More investigation is required to clarify the discrepancy between the results obtained in gas and liquid carrier phases. Specifically, no experimental investigation is found in the literature concerning the effect of particle size on the particulate phase turbulence in horizontal liquid-continuous flows. The current study investigates this relationship ~~between solid phase turbulence and particle size~~ at different flow *Re*.

Another important aspect of two-phase particulate flows is the spatial distribution, or concentration profile, of particles across the channel or pipe. This is particularly important for modeling wear in two-phase pipelines (Shook et al., 1990). In a vertical solid-gas pipe flow, Lee and Durst (1982) carried out several experiments with 100-800 μm particles at $Re \sim 8{,}000$. It was found that small particles are concentrated in a region near the pipe wall while the larger particles mostly accumulate in the core region. They attributed the distribution to the shear-induced lift force (i.e., Saffman force) in the radial direction (Saffman, 1965). The magnitude and direction of this lift force depends on the ~~spatial gradient of~~ relative liquid velocity around the particles. In the near-wall region, the small particles are faster than the surrounding fluid while the larger particles are slower than the surrounding fluid. In the former case, the Saffman force acts towards the wall, while in the latter case (for the larger particles) it acts in the direction of the pipe core. Concentration profiles of buoyant particles at $Re = 5{,}600$ were evaluated using DNS by Picano et al. (2015). Their results showed a generally uniform distribution of particles across the channel except near the wall, where a near-wall local maximum at $y/h \sim 0.03$ and a local minimum at $y/h \sim 0.06$ were observed. In their study, y refers to wall-normal distance and h to the channel height. The investigations showed that the number density and dispersion of the particles across the channel height depends on the carrier phase turbulence and density ratio of solid and liquid phases. However, in general, lighter particles at high Re have a more uniform distribution.

The present study provides a detailed investigation of the effects of particle size, flow Re, and particle concentration on the turbulence statistics of both the liquid and solid phases in a horizontal channel. The St number is employed in the analysis to combine the effect of particle size and flow Re. A combination of PIV and PTV techniques is used for simultaneous measurement of the turbulence statistics of the carrier and particulate phases. The mean velocity profile and Reynolds stresses of the unladen flow are compared with the DNS results of Moser et al. (1999) for evaluation of the measurement system. The measurements are used to obtain turbulence modulation and evaluate the modulation criterion established by Tanaka and Eaton (2008) at higher Re.

2. Experimental Apparatus and Technique

2.1. Slurry flow loop

The experiments are performed in a horizontal slurry flow loop equipped with a centrifugal pump (LCC-M, GIW Industries Inc.) which can circulate up to 2 m^3/min of unladen water. The schematic of the flow loop is displayed in Fig. 1. The test section has a rectangular cross-section of 120 mm (w) width and 15 mm height (h). The channel windows are made of cast acrylic with high quality surface finish of 0.7 μm, which can be considered as a smooth surface. The flow rate is measured using a Coriolis flow meter (Micro Motion, F-series) with mass flow accuracy and repeatability of ±0.10% and ±0.05% of the measured flow rate, respectively. The centrifugal pump is controlled by a variable frequency drive (A510, Teco Electric & Machinery Co., Ltd.) to hold the flow rate

constant during each experiment. The standard deviation of the time series of the flow rate data is less than 0.03% of the average flow rate. The flow loop utilizes two data acquisition cards (NI 9211 and 9263, National Instruments) to record the mass flow rate, temperature and mixture density at a sampling rate of 1 Hz, and to control the variable frequency drive. A double-pipe heat exchanger is used to keep the fluid temperature at 33±0.25 ˚C. The test section has a rectangular cross-section and is 2.5 m long; the measurements are made at a distance of 1.65 m (110*h*) downstream of the channel entrance (as indicated in Fig. 1) to ensure fully developed flow.

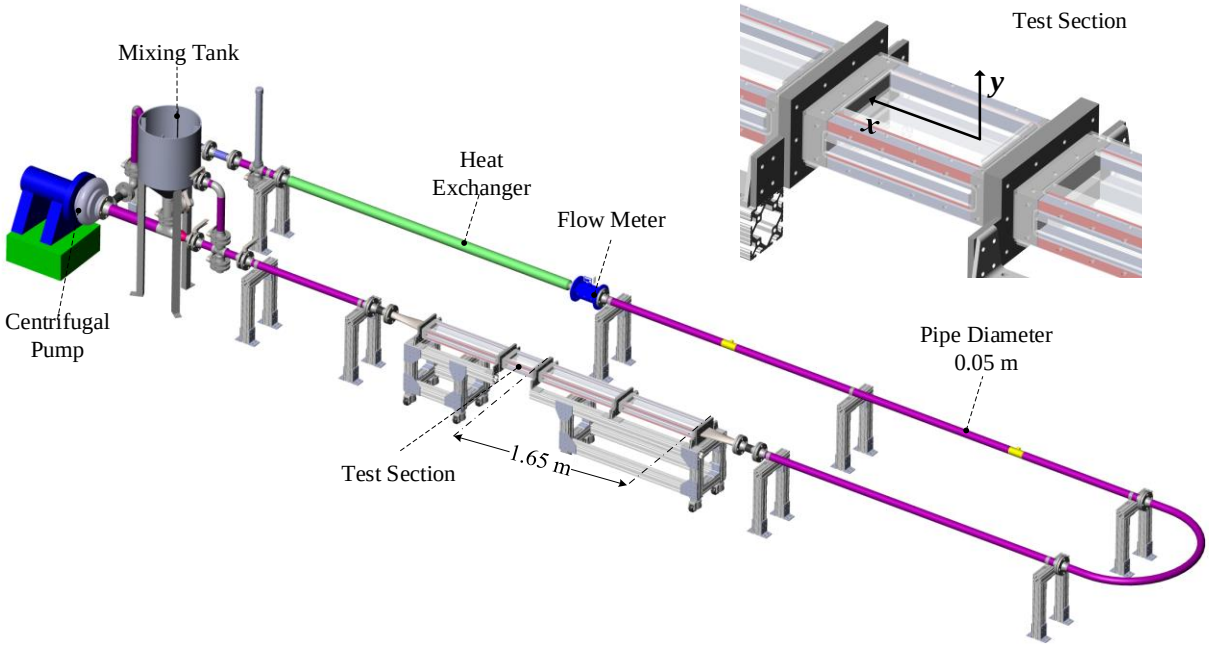

Fig. 1. Schematic of the slurry flow loop equipped with a centrifugal pump and a test-section with rectangular cross-section. A magnified view of the test-section with the streamwise (*x*) and wall-normal (*y*) axis is also shown.

Glass beads with nominal diameters of 285 to 700 μm (Manus Abrasive Systems Inc.) and density of 2670 kg/m^3 were used as the particulate phase. The actual size distribution of each particle type is obtained from the PTV images (detailed in Section 2.2) as shown by the probability density functions in Fig. 2. An estimation of the median diameter (d_p) of the beads is used to indicate the particle size as presented in Table 1. The experiments are conducted at different particle volumetric concentrations (φ_v) and *Re*, as summarized in Table 1. The *Re* is calculated based on the channel height (h) and average velocity (U_{avg}) at the test section. The first row of the table shows the experiments conducted to study the effect of *Re* for different particle sizes. The results of these experiments are detailed in Sections 4.2 and 4.3. The second and third rows of the table present the experimental conditions selected to investigate the influence of particle size and volumetric concentration, which will be discussed in Sections 4.4 and 4.5, respectively.

Table 1
Experimental parameters used in the two-phase experiments to investigate the effect of *Re*, particle size and volumetric concentration.

Objective of the investigation	$Re \times 10^{-3}$	d_p (μm)	φ_v (%)
Effect of *Re*	50, 75, 100, 125	285	0.05
	50, 75, 100, 125	530	0.05
	50, 75, 100, 125	700	0.05
Effect of particle size	50	285, 530, 700	0.05
	125	285, 530, 700	0.05
Effect of φ_v	75	340	0.03, 0.11, 0.18
	125	340	0.03, 0.11, 0.18

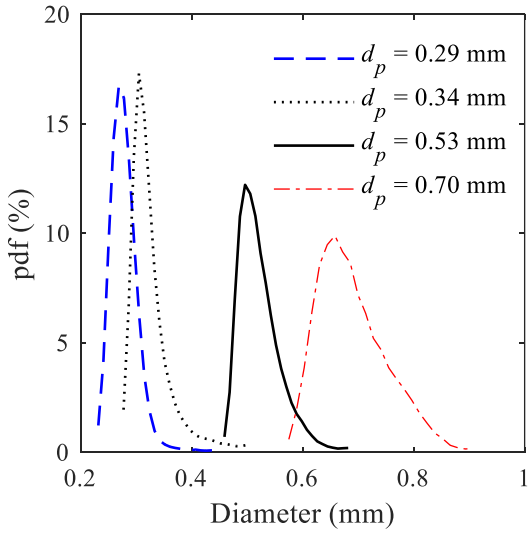

Fig. 2. Size distributions of the four particle types used in the experiments, estimated from the PTV images.

2.2. Particle image and tracking velocimetry

A combined PTV-PIV method is applied here to measure the velocity of the glass beads and the surrounding liquid phase from a common set of images. Methods based on fluorescence tagging (Sridhar and Katz, 1995), intensity discrimination (Anderson and Longmire, 1996), phase dynamics (Delnoij et al., 1999), and geometrical characteristics (Hassan et al., 1992) have been used to discriminate the smaller tracers of the liquid phase from the larger particles (i.e., the solid phase) in image-based measurements. There are specific challenges and limitations associated with each of these methods. For example, fluorescence tagging requires a substantial amount of fluorescent particles for a large-scale experimental setup such as the flow loop used here. Khalitov and Longmire (2002) used the size and intensity of tracers to distinguish them from larger and brighter particles. Kiger and Pan (2000) used a two-dimensional median filter to separate images of particles and tracers. The median filter increases the intensity difference of the tracers and dispersed particles to apply a phase discrimination algorithm. An algorithm based on that of Kiger and Pan (2000) is used here to separate the tracers and the glass beads in the images.

Images are captured using two CCD cameras (Imager Intense, LaVision, GmbH), each with a sensor size of 1040 × 1376 pix, arranged side-by-side to cover a larger streamwise portion of the channel for improved statistical convergence. Each pixel of the CCD is 6.45 × 6.45 μm^2 with 12-bit digital resolution. An Nd:YAG laser (New Wave Research, Solo PIV III) with maximum pulse energy of 50 mJ over 3-4 ns pulse width at 532 nm wavelength is used for illumination. The laser beam is directed into a combination of two spherical lenses and a cylindrical lens to form a 1 mm-thick laser sheet, which illuminates an *x*-*y* plane in the mid-spanwise section of the channel as displayed in Fig. 1. The cameras are equipped with SLR lenses (Sigma) with focal length of f = 60 mm at an aperture diameter of f/16. Each camera lens is aligned normal to the laser sheet and sidewalls to minimize astigmatism and variation of magnification in the images. The FOV of each camera is 11.8 mm by 15.5 mm along the *x*- and *y*- directions, respectively. Overall, for the imaging system, the magnification and digital resolution are 0.57 and 88 pix/mm, respectively. The estimated depth-of-field is about 5 mm, which is greater than the laser sheet thickness. The cameras are synchronized with the laser using a programmable timing unit (PTU9, LaVision, GmbH) controlled by DaVis 7.4 (LaVision, GmbH), acquiring double-frame images at a sampling rate of 3 Hz. The particle displacement between two consecutive frames was set to 20 pixels by adjusting the time interval between the two laser pulses. A large ensemble of 60,000 double-frame images of the two-phase flow was captured for each experimental condition specified in Table 1. The images include the glass beads and the liquid phase seeded with the 2 μm silver-coated glass beads (SG02S40 Potters Industries) with a density of 4 g/cm^3. This large number of images is necessary to capture a sufficient number of particles for improved statistical convergence of PTV results. Only 8,000 double-frame images were used for the liquid phase PIV results.

The PTV algorithm detects and tracks the large glass beads in the double-frame images. The diameter of glass beads in the images varies from 25 pix for 285 μm particles to 60 pix for particles of 700 μm in diameter. The glass beads in the two-phase images are detected using the

'imfindcircle' function in MATLAB (R2015a, MathWorks). This function uses the circle Hough transform to find the circle center and radius (Atherton and Kerbyson, 1999). The beads with average intensity below a threshold value are considered out of the laser sheet and the information is discarded. A sample of the two overlapped frames with the detected glass beads is shown in Fig. 3a. A tracking script developed in MATLAB is used to search for the particle in an area specified by a search radius (20 pix for 285 μm and 30 pix for 700 μm particles) around the predicted position in the second frame. The particle position in the second frame is predicted using an averaged velocity field obtained from an ensemble of the correlation maps (Meinhart et al. 2000). In the next step, two interrogation windows are placed around the particle pair in the first and the second frames as demonstrated in Figs. 3b and c. The interrogation windows are cross-correlated to obtain the displacement of the bead. The area around the perimeter of the glass bead in the first frame is cleared and filled with random noise to minimize the impact of tracers in the cross-correlation. A cross-correlation coefficient with a threshold of 0.85 is used to filter out the pairs that do not have a similar pattern. The wall-normal direction is divided into 150 pix (2 mm) bins with 50% overlap for calculation of the particle mean velocity profile and turbulent statistics. The error analysis for the PTV results of the particles is provided in the appendix section.

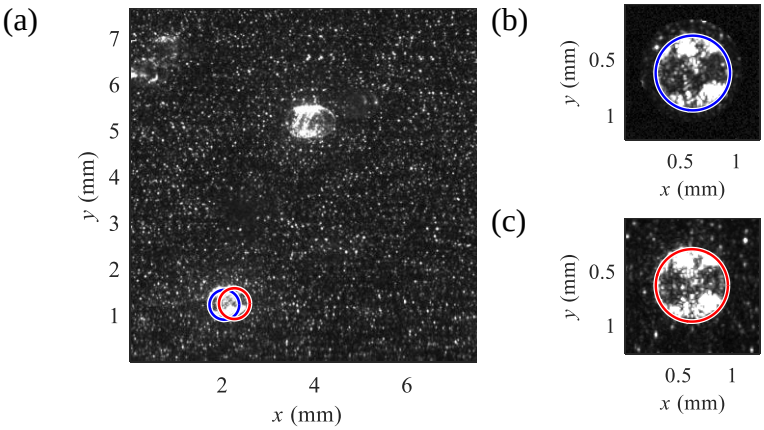

Fig. 3. (a) A sample image of two superimposed frames. The detected pair of glass beads is specified in blue (first-frame) and red (second-frame). (b) The interrogation window around the glass bead of the first frame. The perimeter of the glass bead is filled with random noise. (c) Interrogation window around the glass bead in the second frame includes the surrounding tracer particles.

A PIV algorithm is applied to the two-phase images to obtain the velocity of the liquid phase surrounding the glass beads. The background noise is first removed by subtraction of the minimum intensity of the ensemble of images in order to reduce the laser glare from the wall and stationary image features (Raffel et al., 2007). A median filter is then applied for phase discrimination and to

mask out the glass beads. The filter reduces the intensity of the tracers while the intensity of glass beads remains almost constant. This is indicated in the inverted images of Figs. 4a and b. The image intensity is inverted here for image clarity. The pixels with intensity above a threshold (dark areas in the inverted image) are the glass beads, which are excluded from the cross-correlation algorithm. The kernel size of the median filter depends on the size of the glass beads, but is about 25 × 25 pix in the measurements made in the current study.

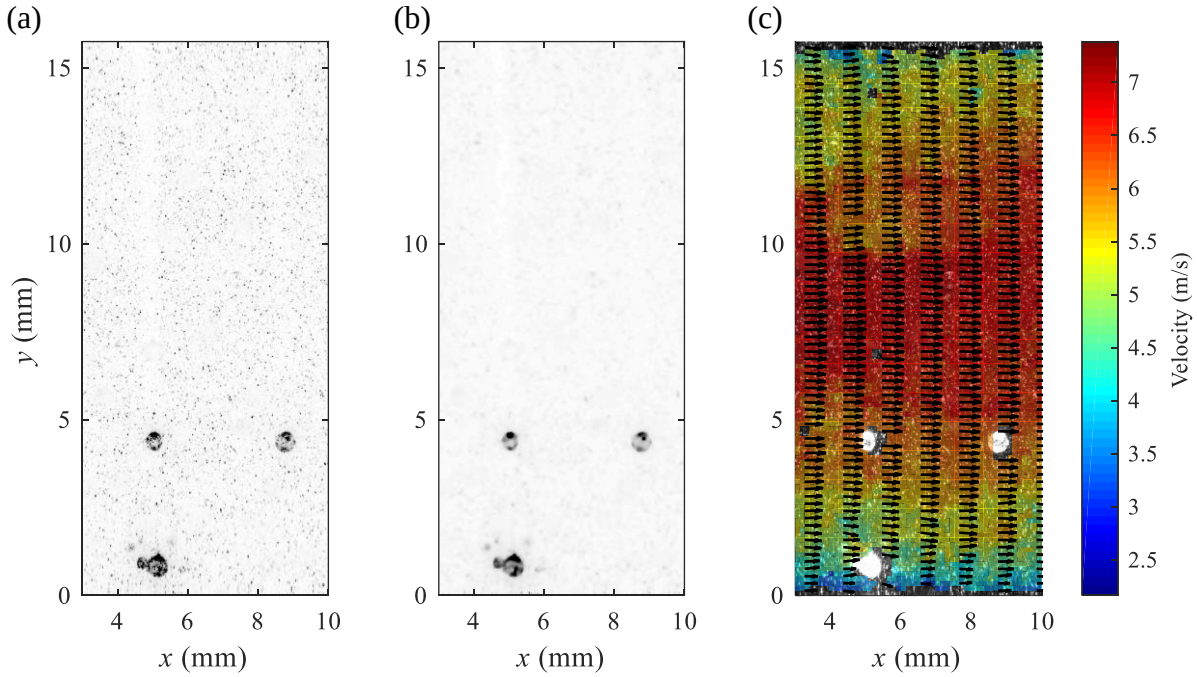

Fig. 4. (a) A sample inverted image after subtracting the sliding minimum. (b) The image after applying the median filter to enhance the contrast of the large glass beads. (c) The velocity field of the liquid phase obtained from the cross-correlation algorithm.

A multi-pass PIV is applied in Davis 8.3 (LaVision, GmbH) to the images with masked-out particles to obtain the fluid phase velocity. The first correlation pass applies an interrogation

window size of 128 × 128 pix and 50% overlap. The window size is reduced to 16 × 16 pix (0.18 × 0.18 mm^2, 0.012h × 0.012h) and 75% overlap in the final cross-correlation pass. The instantaneous vector field obtained from the sample image is shown in Fig. 4c. The white areas represent the pixels occupied by the glass beads. The interrogation windows that contain a masked-out area larger than 1% of the window area are rejected to ensure no bias occurs in liquid phase velocimetry. The instantaneous velocity U in turbulent flow is decomposed into a mean, shown as $<U>$, and a fluctuating component u, where $U = <U> + u$.

3. Flow parameters

The non-dimensional parameters used for presenting and discussing the results are defined here. Measured mean velocity and rms of velocity fluctuations in the two-phase experiments are normalized by the centerline velocity (U_c). The average velocity (U_{avg}) is the average of liquid phase velocity over the channel height at the mid-spanwise plane of the channel, and is used to calculate the *Re*. These parameters are obtained from PIV measurements in the unladen flow and are presented in Table 2. The table also presents the friction velocity, u_τ, and wall-unit, $\lambda = \upsilon/u_\tau$, estimated using the Clauser method (Clauser, 1956) from the measured PIV data. The Reynolds number based on the friction velocity ($Re_\tau = u_\tau h/\upsilon$) is also reported, where υ is the kinematic viscosity of water.

Table 2
The parameters of the unladen flow obtained from PIV measurements detailed in Section 2.2.

Re (×10^3)	Re_τ (×10^3)	U_{avg} (m/s)	U_c (m/s)	u_τ (m/s)	λ (μm)
50	2.4	2.45	2.74	0.12	6.1
75	3.3	3.67	4.08	0.16	4.6
100	4.5	4.89	5.40	0.22	3.3
125	5.5	6.12	6.70	0.27	2.7

Both the flow characteristics and the fluid interaction with the particulate phase are governed by several non-dimensional flow parameters including density ratio, *Re*, and *St*, where *St* is the ratio of the response time of particles to a characteristic time-scale of the flow, typically the integral or Kolmogorov time scale. The integral time-scale (τ_L) is typically computed using the autocorrelation function (Pope, 2000), which is not applicable here, since it requires time-resolved data. Similar to the works of Milojević (1990), Kussin and Sommerfeld (2002), and Brenn et al.

(2003), the integral time-scale is estimated in this study using dimensional analysis (Tennekes and Lumley, 1972) as

$$\tau_L = \frac{1}{3}\frac{\langle u^2 \rangle}{\varepsilon}, \quad (1)$$

where the ε is the turbulence dissipation rate at the channel centerline. The Kolmogorov time scale (τ_K) is defined as

$$\tau_K = \left(\frac{\upsilon}{\varepsilon}\right)^{1/2}. \quad (2)$$

The dissipation rate is calculated as (Milojevié, 1990)

$$\varepsilon = C_\mu^{0.75}\frac{k^{1.5}}{l_m}, \quad (3)$$

using C_μ = 0.09 and $l_m = 0.07h$ (Schlichting and Gersten, 2017). The turbulent kinetic energy k is estimated using (Milojevié, 1990)

$$k = 0.5(\langle u^2 \rangle + 2\langle v^2 \rangle). \quad (4)$$

The ensemble average of the streamwise, $<u^2>$, and wall-normal velocity fluctuation, $<v^2>$, of the unladen flow at the channel centerline is obtained using PIV. The particle response time τ_p, is calculated from

$$\tau_p = \frac{\rho_p d_p^2}{18\mu\, f_d}, \quad (5)$$

where ρ_p is the particle density and μ is the fluid viscosity. The coefficient $f_d = 1.0 + 0.15\,(\rho_f V_s\, d_p/\mu)^{0.687}$ accounts for deviations from Stokes flow (Kussin and Sommerfeld, 2002). Here, ρ_f denotes the fluid density, and V_s is the terminal settling velocity calculated from

$$V_s = \frac{1}{18\mu f_d} d_p^2 g(\rho_p - \rho_f). \quad (6)$$

The calculated values of *St* for the 285, 530, and 700 μm particles at the *Re* values studied here (see Table 1) are presented in Table 3. The settling parameter is defined as the ratio of the terminal settling velocity V_s to the friction velocity, u_τ. When V_s/u_τ is ~ 1, the particles stay in suspension (Sumer and Oguz, 1978). The particle sizes and *Re* numbers considered here are such that a particle bed does not form in the channel: V_s/u_τ values vary from 0.31 for d_p = 285 μm and *Re* = 125,000 to 4.5 for d_p = 700 μm and *Re* = 50,000. It was observed that the particles remain completely suspended in the flow when V_s/u_τ = 0.31, while the particles mostly appear at bottom half channel for V_s/u_τ = 4.5.

Table 3
Calculated values of particle Stokes numbers (*St*) based on the Kolmogorov time scale and the integral time scale (presented in the parentheses).

	Re = 50,000	*Re* = 75,000	*Re* = 100,000	*Re* = 125,000
d_p = 285 µm	4.1 (0.60)	7.5 (0.90)	11.4 (1.19)	15.8 (1.47)
d_p = 530 µm	8.1 (1.18)	14.8 (1.76)	22.5 (2.33)	31.0 (2.89)
d_p = 700 µm	10.6 (1.55)	19.3 (2.31)	29.4 (3.05)	40.6 (3.79)

4. Results and Discussion

In this section, first measurement in the unladen flow is compared with the DNS results of Moser et al., (1999) for an uncertainty evaluation of the PIV system. The subsequent sub-sections investigate the effect of *Re*, particle size and concentration on the turbulence intensity of the solid and liquid phases. The observations are discussed and compared with previous studies reported in the literature (e.g., Kiger and Pan, 2002; Shokri et al., 2017; Varaksin et al., 2000; Zhao et al., 2015). The velocity and turbulence intensity results are plotted for the bottom half of the channel due to its higher solids concentration and more relevance to industrial applications.

4.1. Unladen turbulent channel flow

The mean velocity profile and turbulence intensities of the unladen flow at *Re* of 20,000, 40,000 and 75,000 are compared with DNS of Moser et al. (1999) in Fig. 5. The *Re* of the unladen flows are selected based on the availability of DNS data but they are also within the range of *Re* of two-phase flow experiments. The figures are normalized using the channel height and centerline velocity. This outer layer scaling (h and U_c) is selected since spatial resolution of the PIV system is selected to measure the full channel. The mean streamwise velocity profiles are in agreement with the DNS results in the bottom-half of the channel as shown in Fig. 5a. The discrepancy between the DNS and the experimental results is smaller than 1.0% at $y/h > 0.025$. The figure also reveals that the maximum velocity is also located at $y/h = 0.5$ that shows the symmetry between the top and bottom half of the channel.

The streamwise turbulence intensity, $<u^2>/U_c^2$, of Fig 5b agrees with the DNS results at $y/h > 0.1$ with a maximum discrepancy of 4.0%. The discrepancy closer to the wall is due to the limited spatial resolution of the PIV system. The PIV measurements of the wall-normal Reynolds stress, $<v^2>/U_c^2$, in Fig. 5c are smaller than the DNS values. This figure indicates a systematic bias error with underestimation of approximately 8.5% at $y/h = 0.1$ at *Re* = 75,000. The difference decreases approaching the channel centerline since turbulent scales become larger. The spatial averaging within the interrogation window in the PIV measurement causes an underestimation of the turbulence intensities since the turbulent energy contribution from small scale eddies is not

resolved (Lee et al., 2016). The ratio of interrogation window size to the Kolmogorov scales rises with the increase of the Reynold number. Hence, the missing small-scale energy due to spatial resolution is larger at higher *Re*. The Reynolds shear stress profiles of Fig. 5d show agreement with DNS results at $y/h > 0.15$ where the profile is linear. A discrepancy is observed closer to the wall with the deviation of 10% at $y/h = 0.1$.

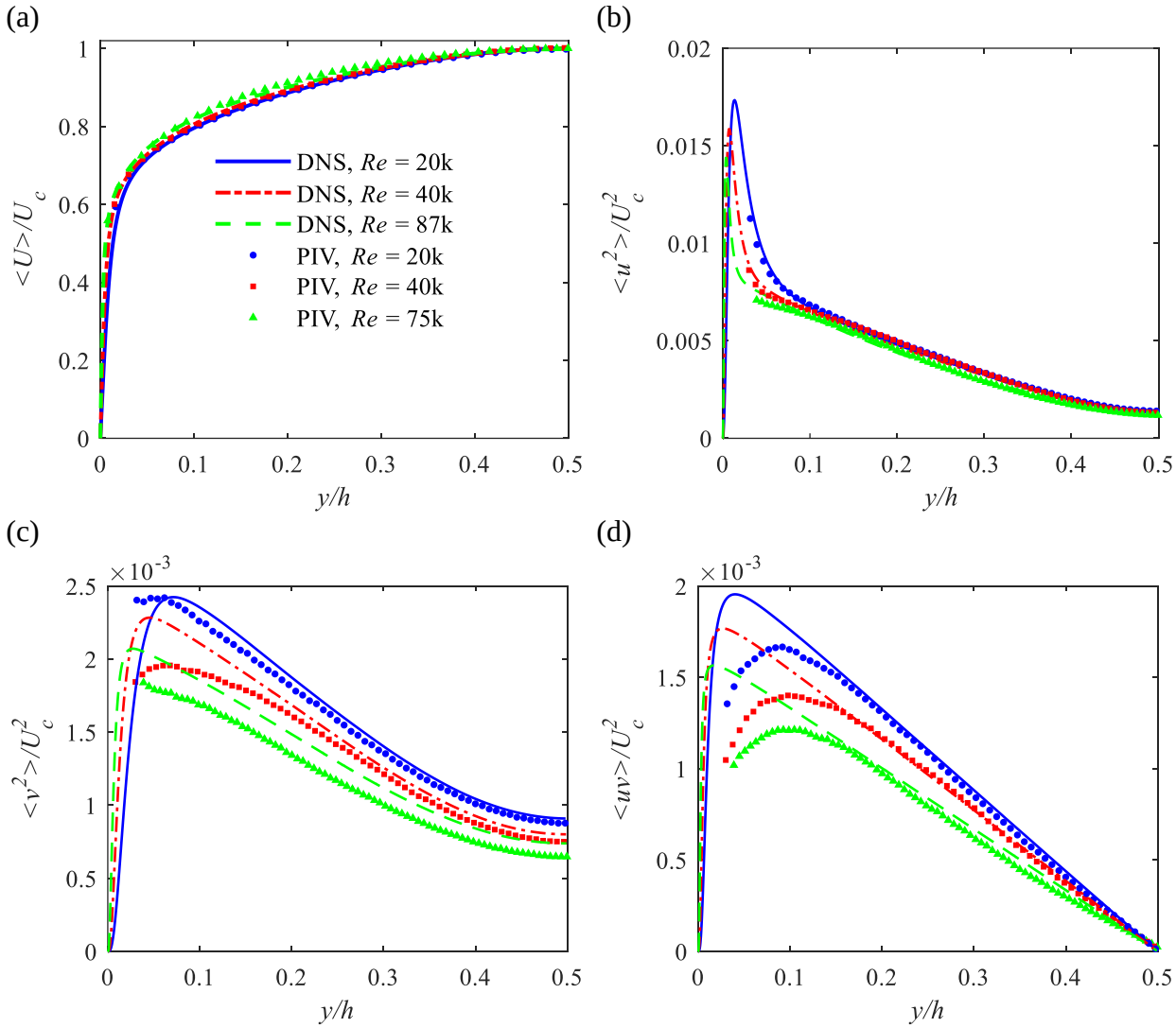

Fig. 5. Profiles of normalized (a) mean streamwise velocity, (b) streamwise turbulence intensity, (c) wall-normal turbulence intensity, and (d) Reynolds shear stress. The lines represent the DNS data at *Re* = 20,000 (Re_τ = 1,080), *Re* = 40,000 (Re_τ = 2,010), and *Re* = 87,300 (Re_τ = 3,990). The symbols indicate the PIV measurement results at *Re* = 20,000 (Re_τ = 1,090), *Re* = 40,000 (Re_τ = 2,000), and *Re* = 75,000 (Re_τ = 3,280). Only one out of two data points is presented for clarity of the plots.

The assessment of the deviation of PIV measurements from the DNS data shows that measurement of $\langle u^2 \rangle$ is reliable at $y/h > 0.1$, with an uncertainty smaller than 4.0%. The smaller displacement of the tracers in wall-normal direction in the double-frames PIV images increases the relative error

in statistics that include the *v* component. Therefore, the investigation of the wall-normal turbulent intensity and the Reynolds shear stress of the liquid-phase are restricted to $y/h > 0.15$ in the next sections.

4.2. Effect of *Re* on mean velocity

This section investigates the effect of *Re* on the mean velocity profile of the liquid and particulate phases. The normalized streamwise and wall-normal mean velocity profile of the glass beads and the carrier phase at the bottom half-channel are plotted in Figs. 6a, b, and c for the three particle diameters of 285 μm, 530 μm and 700 μm, respectively. The results are presented for the bottom half because most of the beads were found in this region, and thus the computed statistics are more reliable. Each figure shows velocity profiles of liquid and solid phases for *Re* of 50,000, 75,000, 100,000 and 125,000, as well as the streamwise velocity of the unladen flow. In general, the impact of particles on the mean velocity profile at the investigated concentration is negligible and the profiles of the liquid phase and the unladen flow are essentially identical. However, the velocity of the carrier phase and the particles are different, as discussed below. The wall-normal velocity profiles also indicate that the net wall-normal velocity is negligible compared to the streamwise component of velocity, and the glass beads stay in suspension.

Figure 6 shows that the relative velocity of the liquid and particulate phase depends on both the *Re* and particle size. Scrutiny of Fig. 6 reveals that the mean velocity of $d_p = 285$ μm particles at all *Re* is smaller than the velocity of the liquid phase at $0.03 < y/h < 0.5$ where reliable data for the particulate phase is available. For larger particles of $d_p = 530$ and 700 μm, the mean velocity is smaller than the unladen liquid only at the lowest *Re* of 50,000 in the specified region. In other words, at higher *Re*, only the small particles have a mean velocity lower than that of the carrier phase, while all the particles exhibit a finite (nonzero) mean slip velocity at the lowest *Re* tested here. The observed lag is due to the preferential accumulation of the beads in low-speed regions. It has been shown by Kiger and Pan (2002) and Hout (2011) that most of the upward-moving beads (ejection motion) are located in low-speed regions, while downward-moving beads (sweep motion) are distributed more evenly over high-speed and low-speed flow regions. However, it is noteworthy that the glass beads in the aforementioned cases might lead the fluid in the near-wall region ($y/h < 0.03$).

In the high velocity region of the channel ($y/h > 0.3$), the particles are slower than the liquid phase at all flow *Re* tested here. This lag in particle velocity decreases as the *Re* increases, consistent with the results of Rashidi et al. (1990) in the liquid-continuous flow in a horizontal channel and those of Shokri et al. (2017) in the liquid-continuous flow in vertical pipe. In the near-wall region, the larger particles lead the liquid phase. For example, the 700 μm particles of Fig. 6c have higher mean velocity than the fluid phase at $y/h < 0.25$ for $Re = 100{,}000$ and larger. The same result was found in upward pipe flow by Shokri et al. (2017), and has been associated with the large wall-normal displacement of high velocity glass beads from the center of the channel to the near-wall

region (Vreman, 2015). The larger particles travel a longer distance in the wall-normal direction and preserve their momentum for a longer time, due to their larger *St*.

The point at which the velocity of the particle and the liquid phase are the same is called the crossing point and is indicated by the '*' symbols in Fig. 6. No crossing point is detected in the region $0.03 < y/h < 0.5$ for the 285 μm particles at Re = 50,000 as the particle velocity is smaller than the liquid phase across the measurement range. As the particle size and Re increase, St also increases, and the crossing point moves away from the wall. A similar trend was observed by Shokri et al. (2017) in an upward solid-liquid pipe flow, while Lee and Durst (1982) observed that the crossing point moves closer to the wall as the particle size increases in a solid-gas flow. This highlights the different behavior of particles in liquid and gas flows. Increasing the St (by increasing particle density or diameter) in gas flows reduces the particulate phase velocity across the whole conduit cross-section, which moves the crossing point towards the wall (Kulick et al., 1994; Lee and Durst, 1982). However, with increase of St, the particulate phase velocity increases in the near-wall region for solid-liquid flows, and the crossing point moves away from the wall.

The particle Reynolds number is a critical parameter in evaluating the turbulence modulation and is defined here as $Re_p = |<U> - <U_p>|d_p/\upsilon$. This parameter is computed using the mean velocities of the liquid and solid phases and is shown in Fig. 7a, b, and c for d_p = 285, 530, and 700 μm particles, respectively. As expected, Re_p is larger for larger particles and decreases with increase of flow Re at $y/h > 0.3$ where the particle velocity is lower than that of the fluid. However, the influence of flow Re on Re_p is more pronounced for the larger particles of Fig. 7b and c. A large increase in Re_p (and the relative velocity) is observed for the larger particles of Fig 7c at wall-normal distances at $y/h \leq 0.1$. The Re_p changes from 11 at Re = 50,000 and reaches a maximum value of 225 for Re = 125,000 in this region.

The suspended particles can augment or attenuate liquid phase turbulence over different length scales (Balachandar and Eaton, 2010), which can be discussed in terms of Re_p. Taneda (1956) investigated the wake of a sphere as it moved through a tank of water. It was observed that when the $Re_p < 22$, the flow around the sphere is completely laminar and no vortices can be found. As Re_p increases to about 24, a pair of stationary vortices appear in the wake. They stated that the vortices grow and stretch along the flow direction as Re_p increases. The vortices start oscillating when Re_p of 130 is reached while they are still attached to the sphere. At larger Re_p vortex shedding occurs behind the particle and enhances the liquid phase turbulence. On the other hand, attenuation of liquid phase turbulence occurs due to turbulence dissipation at smaller scales. The overall modulation of turbulence in the liquid phase relies on the relative strength of the vortex shedding and the dissipation mechanisms.

(a) (b) (c)

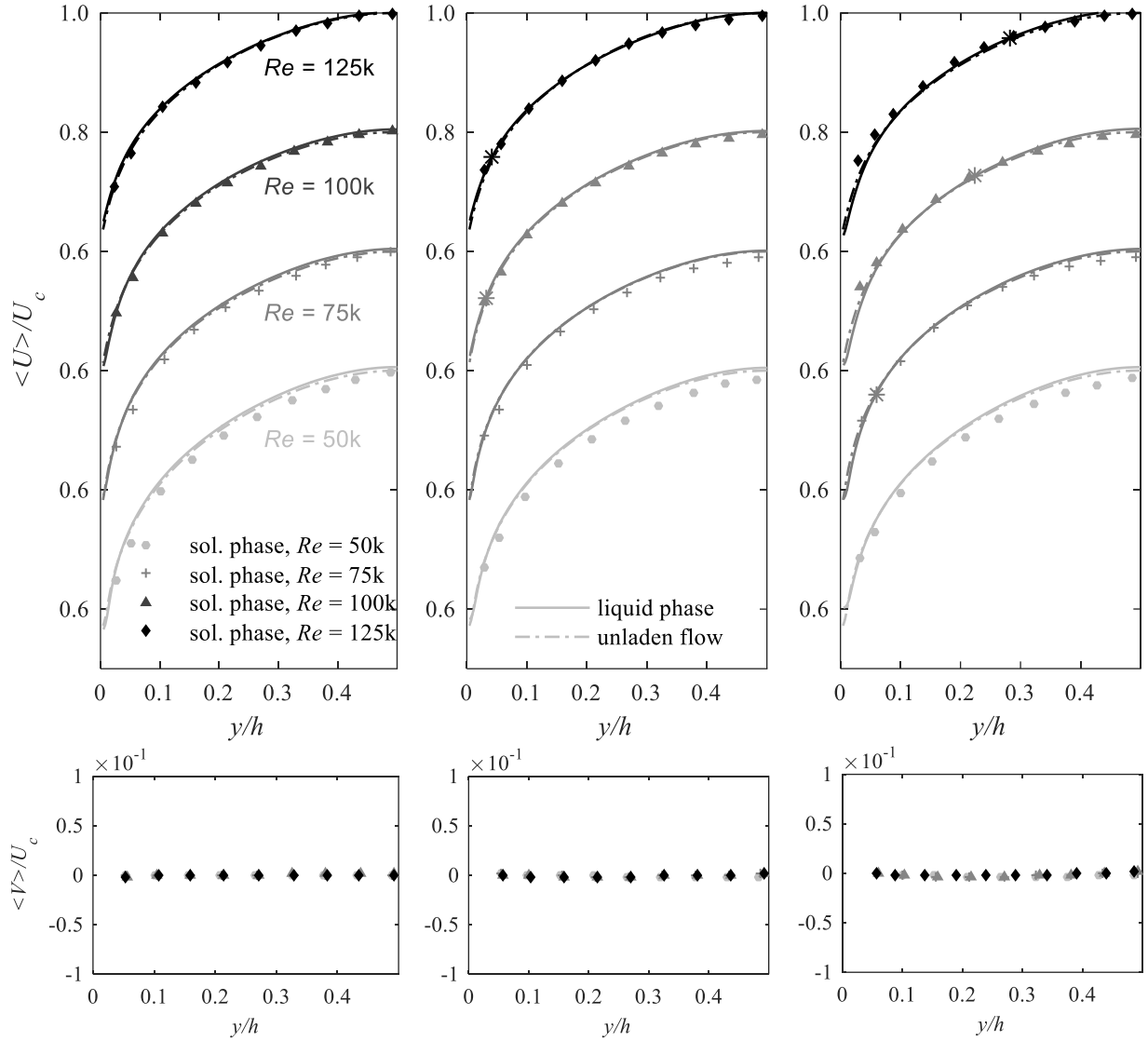

Fig. 6. Mean streamwise and wall-normal velocity profile of liquid phase and the dispersed phase of (a) 285 μm, (b) 530 μm and (c) 700 μm glass beads. The profiles are shown for four Reynolds numbers of Re = 50,000, 75,000, 100,000, 125,000 that are discriminated using different shades. The normalized streamwise mean velocity profile changes from almost 0.6 near the wall to 1.0 at the centerline. The data of the four Re are separated by shifting the profiles upward by an increment of $0.2U_c$.

(a) (b) (c)

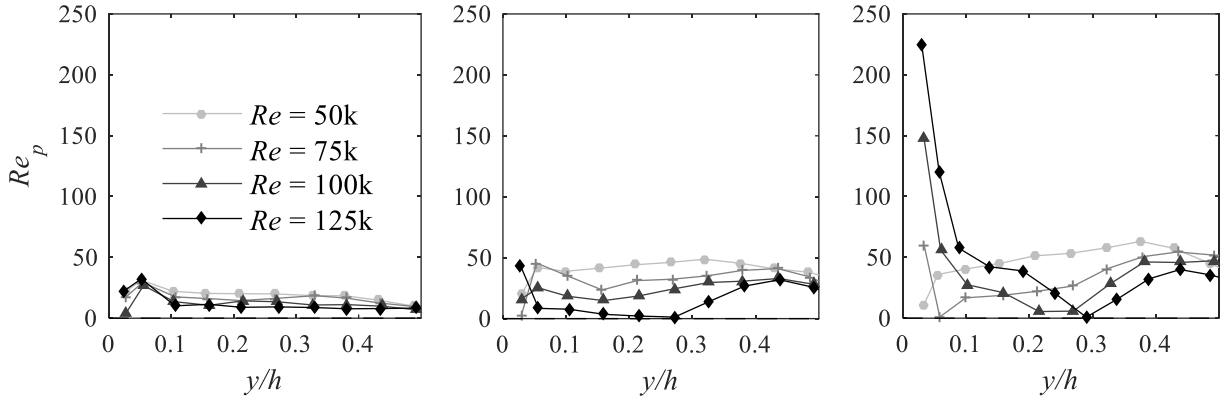

Fig. 7. Particle Reynolds number across the channel based on the mean relative velocity ($<U>-<U_p>$) for (a) 285 μm, (b) 530 μm, and (c) 700 μm glass beads at different ***Re.***

The average of instantaneous slip velocity, defined as $<|U-U_p|>$, is a more accurate representative of mean slip velocity for computing Re_p, relative to the difference between the average velocity of the liquid and particulate phase ($<U>-<U_p>$). Computing $<|U-U_p|>$ requires measurement of liquid velocity, with high spatial resolution, in the immediate vicinity of the glass beads, which is not available from the current PIV/PTV. Due to preferential accumulation of glass beads in the low-speed streaks, Fig. 7 can slightly overestimates Re_p. Lelouvetel et al. (2009) observed that around 60% of 200 μm glass beads at Re = 30,000 are aggregated in the low-speed regions of the flow. However, distribution of glass beads over high-speed and low-speed regions is expected to be more uniform in the current experiment, since particle aggregation in low-speed streaks reduces with St (Marchioli et al. 2003).

4.3. Effect of *Re* on turbulence and particle distribution

The effect of Re on streamwise turbulence of the liquid and solid phases at the bottom half of the channel is shown in Fig. 8a and b for d_p = 285 and 700 μm particles, respectively. The streamwise turbulence of the unladen flow at the same Re is also shown for comparison. In general, the streamwise turbulence intensity of the liquid in the two-phase flow is slightly larger than the unladen flow. Therefore, turbulence production by the vortex oscillation is stronger than the dissipation of turbulence. For the 700 μm particles, which are associated with larger values of Re_p, the vortex shedding augmentation mechanisms are stronger and a slightly larger difference is observed between the turbulence intensity of the liquid phase in the two-phase flow and the unladen flow. The wall-normal turbulence intensities of both the solid and liquid phases for d_p = 285 μm and d_p = 700 μm particles are shown in Figs. 9a and b, respectively. The level of bias error in the $<v^2>$ profiles estimated through comparison with the DNS data is shown by the error bars in the figure for Re of 50,000 and 75,000. The augmentation in wall-normal turbulence is relatively large; the addition of glass beads increases $<v^2>$ of the liquid phase up to two times that of the unladen flow. The largest increase in liquid phase wall-normal intensity occurs for the two-phase flow with the 700 μm particles.

The streamwise turbulence intensities of the d_p = 285 μm particles (shown in Fig. 8a) and d_p = 700 μm particles at *Re* of 50,000 as shown in Fig. 8b are larger than the carrier liquid phase. Due to the larger inertia of the particles, they maintain their streamwise velocity longer than the fluid when transported in the wall-normal direction. This results in larger streamwise velocity fluctuations of the particulate phase (Kulick et al., 1994). Comparison with $\langle u^2 \rangle$ shows the wall-normal turbulence intensity of the particulate phase is smaller than the liquid phase intensity (see Fig. 9a). Similar results were found by Kulick et al. (1994) and Varaksin et al. (2000) in downward air-solid flow and also in horizontal channel air-solid flow by Sommerfeld (2003) and Zhao et al. (2015). The power spectra of the streamwise and wall-normal velocity show that the *v* fluctuation occurs at higher frequency than the streamwise fluctuations (Kulick et al., 1994; Zhao et al., 2015). Therefore, the smaller $\langle v^2 \rangle$ of the particles is associated with lack of response of the particles to high-frequency wall-normal fluctuations of the fluid. This is consistent with the smaller wall-normal turbulence intensity of the larger 700 μm particles in Fig. 9b relative to that of the smaller particles in Fig. 9a.

Figures 8 and 9 also show that $\langle u^2 \rangle$ and $\langle v^2 \rangle$ of the particles decrease with increase of flow *Re* and also by increase of particle diameter. The larger *Re* results in a smaller flow time-scale and consequently larger *St*. Larger particles also indicate a longer response time and larger *St*, as observed in Table 3. Therefore, increase of *St* reduces the turbulence of the particles. This agrees with the results of Shokri et al. (2017) regarding the variation of $\langle u^2 \rangle$ versus particle size. When *St* is large, the response of the particle to carrier phase fluctuation decreases and transfer of turbulent kinetic energy to the glass beads is reduced. Hence, the turbulence intensity of particles is reduced with increase of *Re* and particle size (increase of *St*).

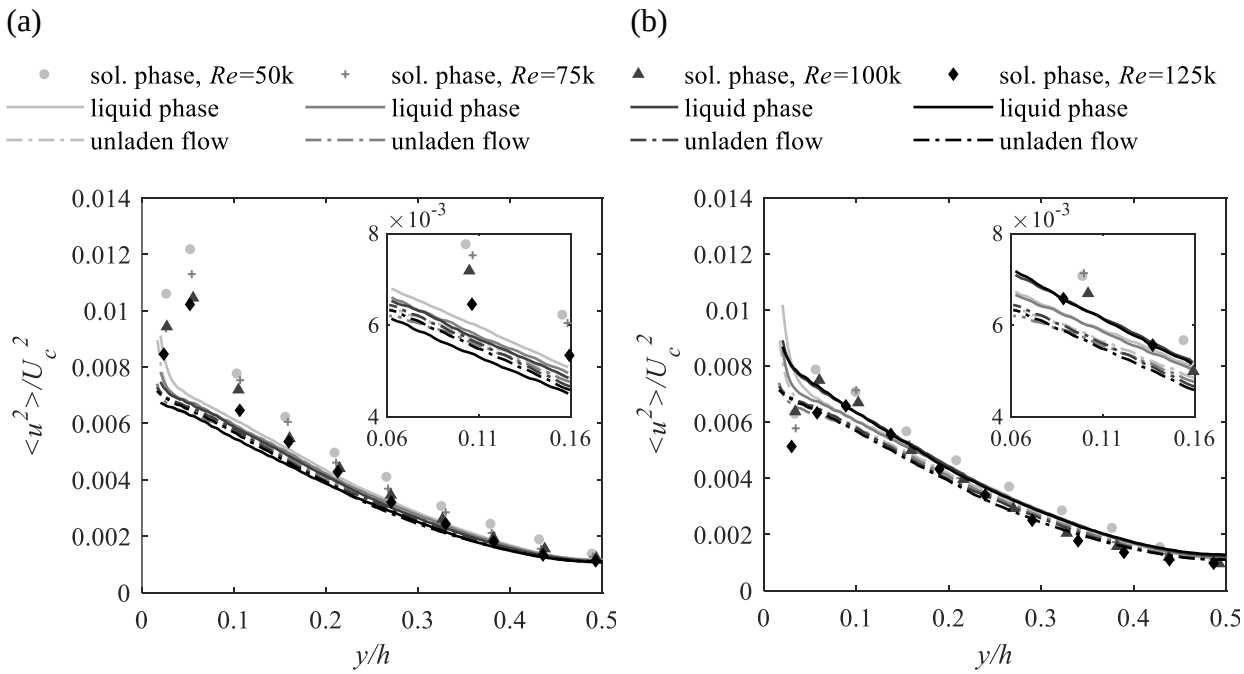

Fig. 8. Streamwise turbulence intensity of the carrier and solid phases in flow with (a) d_p = 285 μm and (b) d_p = 700 μm particles. The statistics of the unladen flow at the same *Re* is also shown for comparison.

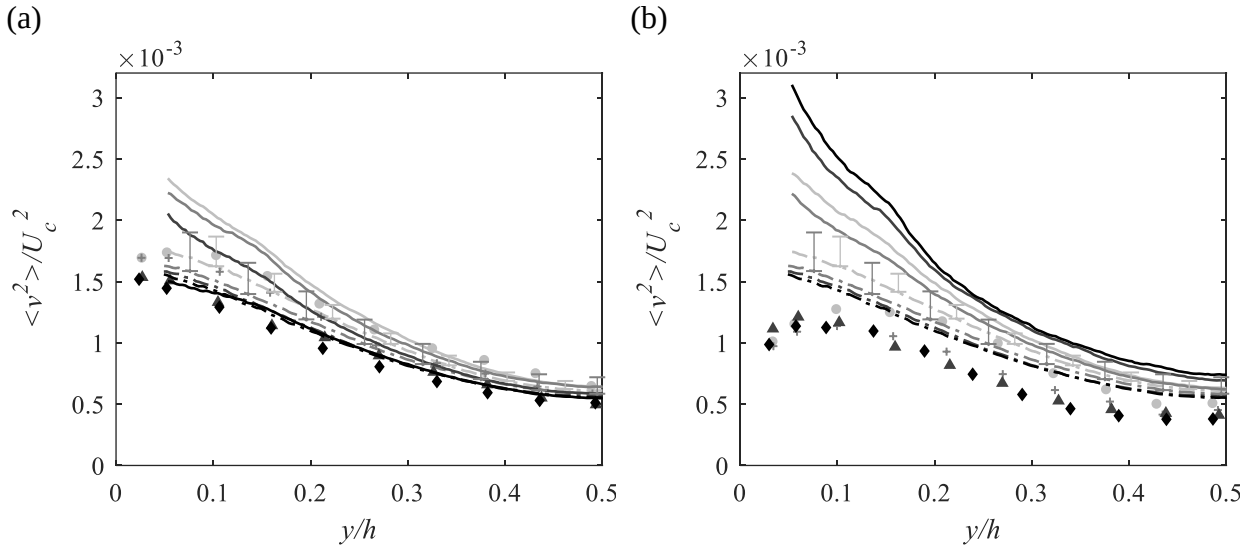

Fig. 9. Wall-normal turbulence intensity of the carrier and solid phases in flow with (a) 285 μm, and (b) 700 μm particles. The statistics of the unladen flow at the same *Re* is also shown for comparison. For legends, see Fig. 8.

The DNS results of Zhao et al. (2015) showed an opposite trend for variation of particle streamwise turbulence intensity with *St*. They studied gas-solid flow in a horizontal channel at low *Re* (*Re* ~ 4,200) and compared the turbulence intensity of 96 μm particles with densities of 225 and 1350 kg/m^3 density at a volumetric concentration of 0.0073% (about ten times lower than the concentration used in this study). Their results revealed that heavier particles with larger *St* have higher streamwise turbulence intensity. The same result as Zhao et al. (2015) was obtained by Kussin and Sommerfeld (2002) at *Re* of 42,500 and Kulick et al. (1994) at *Re* = 13,800, for particle sizes ranging from 50 to 190 μm. The two aforementioned studies also involved solid-gas flows at lower *Re* and smaller particle size than the current study, which caused their *St* to be one to two orders of magnitude smaller than those of the current study. This implies that there should be a critical Stokes number St_{cr} characterizing these two regimes. Turbulence intensity of the solid phase increases with *St* for $St < St_{cr}$, and decreases for $St > St_{cr}$.

The Reynolds shear stress profiles are shown in Fig. 10a and b for the 285 μm and 700 μm particles, respectively. The maximum Reynolds shear stress of the particles occurs at *y/h* ~ 0.1, and in general they have larger $<uv>$ than the liquid phase. This is associated with the larger inertia of the glass beads, which allows them to maintain a higher correlation between the *u* and *v* fluctuations. Figure 10 also shows that, as the *Re* increases, the Reynolds stress of the particles is

reduced across $0.1 < y/h < 0.5$. The reduction is associated with the attenuation of the streamwise and wall-normal Reynolds stress of the particles as shown in Figs. 8 and 9.

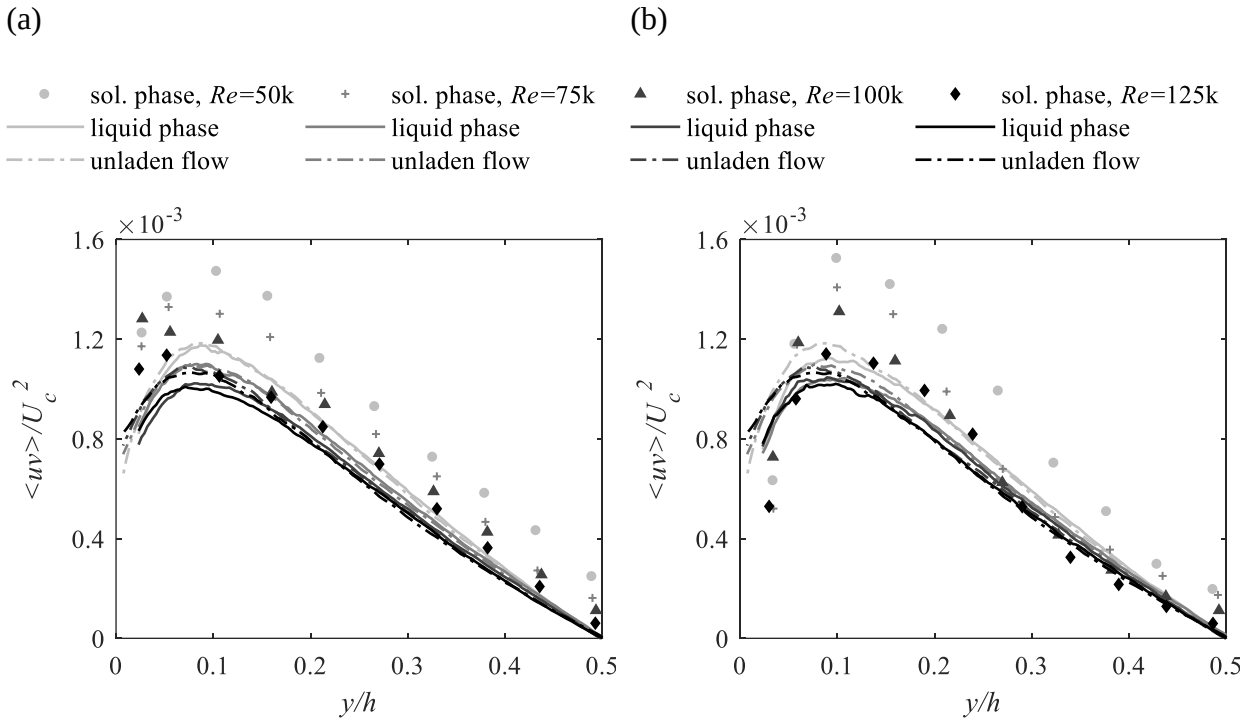

Fig. 10. Reynolds shear stress of the liquid and solid phases in flow with (a) 285 μm, and (b) 700 μm particles. The statistics of the unladen flow at the same *Re* is also shown for comparison.

The distribution of glass beads across the entire channel at various *Re* is indicated in Fig. 11a for d_p = 285 μm and in Fig. 11b for d_p = 700 μm particles. The channel height is divided into 50 pix (Δy_{bin} = 0.57 mm, 0.004*h*) bins with zero overlap, and the number density profiles are computed as the ratio between the number of particles in each bin (N_i) and the average number of particles in the bins (N_{avg}). The profiles are not dependent on the bin size because of normalization by N_{avg}, and the area under each plot is equal to unity. The number density is larger in the near-wall region for the low *Re* cases. This is associated with the larger ratio of the settling velocity to the friction velocity, which indicates poorer dispersion of the glass beads across the channel. With increasing *Re*, turbulence dispersion becomes stronger, which results in more uniform distribution of particles. A local maximum also appears at $y/h \sim 0.4$ for 700 μm particles at the highest *Re* tested (*Re* = 125,000). Smaller wall-normal bead velocities compared to the streamwise component as represented in Fig. 6 indicates the beads distributions are in equilibrium state. Figure 9 also indicates that the $\langle v^2 \rangle$ of the particles is $\sim 0.04 U_c$, while the maximum observed wall-normal settling velocity is $\sim 5\times10^{-3} U_c$. The Comparison of these two values reveals that turbulence in the flow can disperse the beads and bring them into suspension.

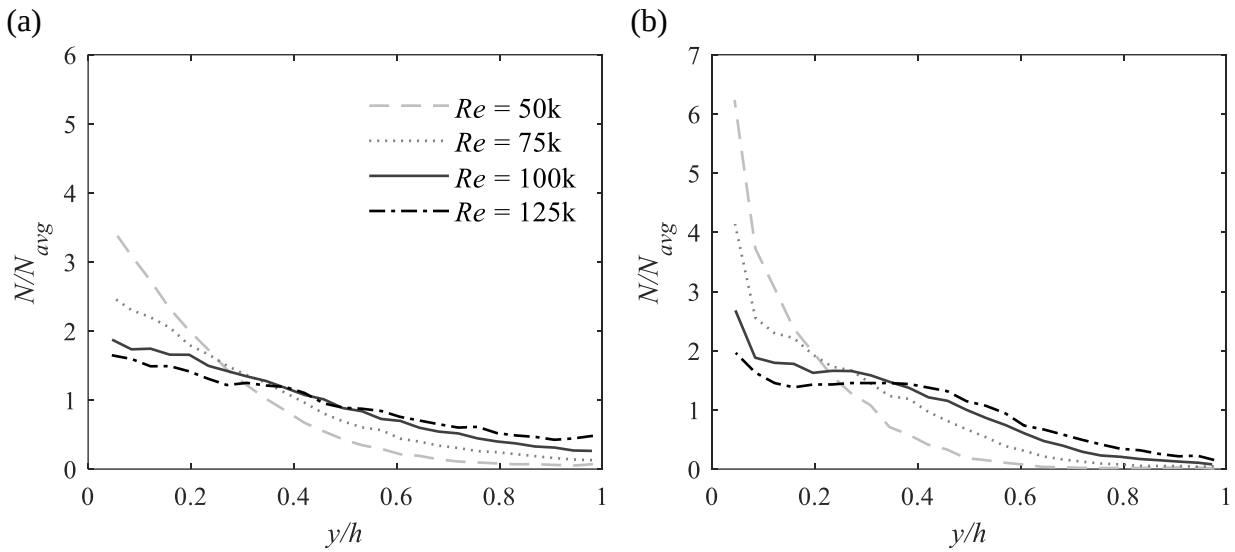

Fig. 11. The number density distribution for (a) 285 μm particles, and (b) 700 μm particles at *Re* varying from 50,000 to 125,000. The plots show the number of particles detected in each bin normalized by the average number of particles in all the bins (N_{avg}).

4.4. Effects of particle size on turbulence and particle distribution

The influence of particle size on the statistics of the liquid and solid phases at the bottom half of the channel as well as the particle distribution across the entire channel are studied in this section for the experimental conditions mentioned in the second row of Table 1. It was observed in Fig. 6 that the effect of particle size on the mean velocity of the liquid phase is negligible, while it has a stronger effect on the solid phase velocity profile especially near the wall. Increasing the particle size from 530 μm to 700 μm at *Re* of 100,000 and 125,000 flattens the velocity profile and moves the cross-over point (indicated by '*') toward the center of channel. The variation of the streamwise turbulence intensity of solid and liquid phases with the particle size can be seen in Fig. 12a for *Re* = 50,000, and in Fig. 12b for *Re* = 125,000. Smaller particles have larger streamwise turbulence intensity. The same trend is observed in Fig. 13 for the wall-normal turbulence intensity. It was explained in Section 4.3 that smaller particles lead to smaller *St* and relaxation time; hence, they are more responsive to the velocity fluctuation of the liquid phase. The turbulent eddies exert a force on the particle and, consequently, part the energy of the eddy will be transferred to the particle. This results in increase of the turbulence intensity of the particulate phase (Gore and Crowe, 1989).

Figures 12 and 13 show that the difference between $<u^2>$ and $<v^2>$ of the liquid phase in particle-laden and unladen flow are larger in the case of the 700 μm glass beads at *Re* = 125,000. This is attributable to the larger Re_p of this case with an average value of ~60 over the bottom half of the channel. It is observed in Fig. 12 that the $<u^2>$ of particles is reduced significantly with the increase of particle diameter (or *St*) at $y/h < 0.1$. The flow has a smaller time scale in this region

than the central region, and the difference between the local *St* of different particles is more pronounced (Righetti and Romano, 2004). It can be seen that $<u^2>$ and $<v^2>$ for the 530 μm and 700 μm particles overlap at $y/h > 0.1$ while the 285 μm particles still have moderately larger turbulence intensity. This is related to the fact that the 530 μm and 700 μm particles have similar *St*, whereas 285 μm particles have considerably smaller *St* as seen in Table 3.

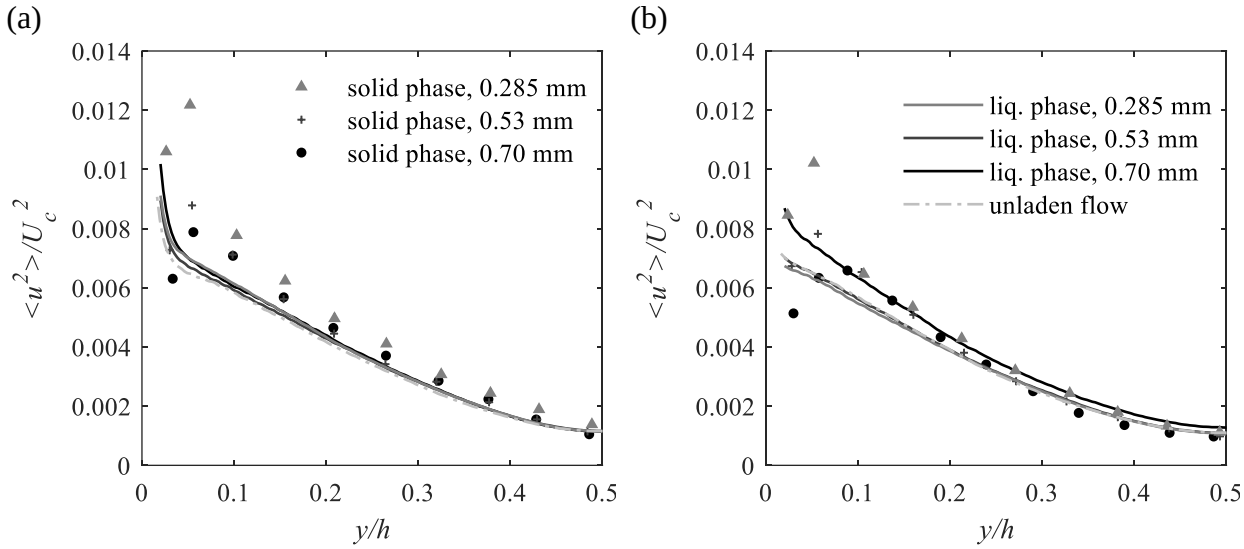

Fig. 12. The streamwise turbulence intensity of the solid and liquid phases at (a) *Re* = 50,000 and (b) *Re* = 125,000 for d_p = 285 μm, 530 μm, 700 μm particles. The streamwise turbulence intensity of the unladen flow is also shown for comparison.

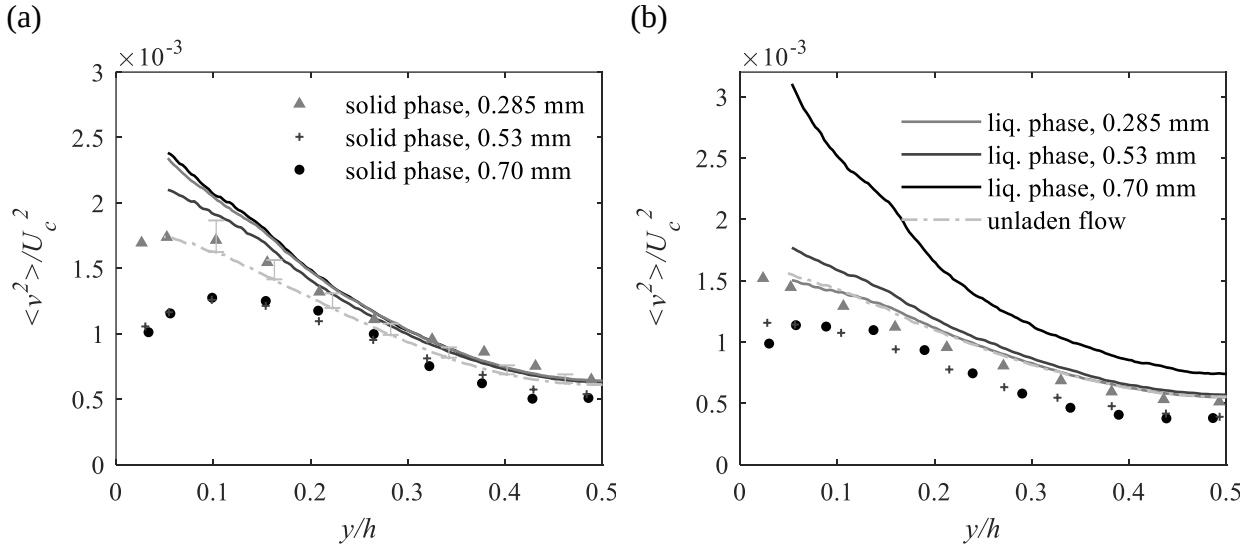

Fig. 13. The wall-normal turbulence intensity of the solid and liquid phases at (a) *Re* = 50,000 and (b) *Re* = 125,000 with d_p = 285 μm, 530 μm, 700 μm particles. The expected underestimation is also shown using error bars for unladen flow at *Re* = 50,000.

The number density distribution of the three sizes of glass beads is shown in Figs. 14a-c for *Re* of 50,000, 100,000 and 125,000, respectively. The number density at $y/h < 0.15$ increases with increasing particle size because of the associated increase in particle settling velocity. The figures also show a clear difference for the largest particle size at *Re* = 100,000 and 125,000; a local minimum appears at $y/h \sim 0.15$. The number density at the local minimum also decreases with the increase of *Re* as shown in Fig. 11b. The local minimum for the d_p = 700 μm particles at *Re* = 125,000 in Fig. 14c is indicated by the '*' symbol. A local maximum also appears at greater distance from the wall ($y/h \sim 0.3$). The number density of the particles increases at the local maximum with the increase of particle size.

The distribution of the particles across the channel cross-section depends on the forces acting on the particles in the wall-normal direction. The drag force, shear-induced lift force (Saffman, 1965), gravity, and turbophoresis forces have been shown to be the most important forces in particle-laden turbulent flows (Li et al., 2016, 2001; Marchioli et al., 2003). The Saffman lift force is proportional to the particle diameter, fluid velocity gradient, and the relative velocity between the fluid and particle. The DNS of Li et al. (2016) in particle-laden gas flow over a flat plate at $Re = U_\infty x/\upsilon = 3.9 \times 10^5$ (U_∞ is the free stream velocity and x is the distance from the edge of the plate) showed that the lift force on 320 μm particles is effective near the wall and becomes negligible at $y^+ \sim 25$ since the velocity gradient is significantly reduced with wall-normal distance. Therefore, the appearance of the local minimum in the particle concentration profile is not attributable to lift force; for example, at $y/h \sim 0.15$ in Fig. 14c, the wall-normal velocity gradient of the fluid phase is small. The interaction of particles with the non-isotropic turbulence causes turbophoresis (Caporaloni et al., 1975; Reeks, 1983), defined as the tendency of particles to migrate in the direction of decreasing turbulence (Marchioli and Soldati, 2002). The turbophoretic force acting on the particles in the wall-normal direction is proportional to $\rho_p V_p \, d\langle v^2 \rangle/dy$, where V_p is the particle volume and the term $d\langle v^2 \rangle/dy$ shows the gradient of wall-normal velocity fluctuation for the particles (Caporaloni et al., 1975). The magnitude of this force increases with increasing particle size and also increase in $\langle v^2 \rangle$ of particles with increasing flow *Re*. It is observed in Figs. 13b that $d\langle v^2 \rangle/dy$ becomes almost zero at $y/h \sim 0.15$ for the 700 μm particles. Therefore, the turbophoretic force is toward the channel center at $y/h > 0.15$, while it changes direction and pushes the particles toward the wall for $y/h < 0.15$. The change in the direction of turbophoretic force seems the most probable factor that causes the local minimum point in Fig. 14c.

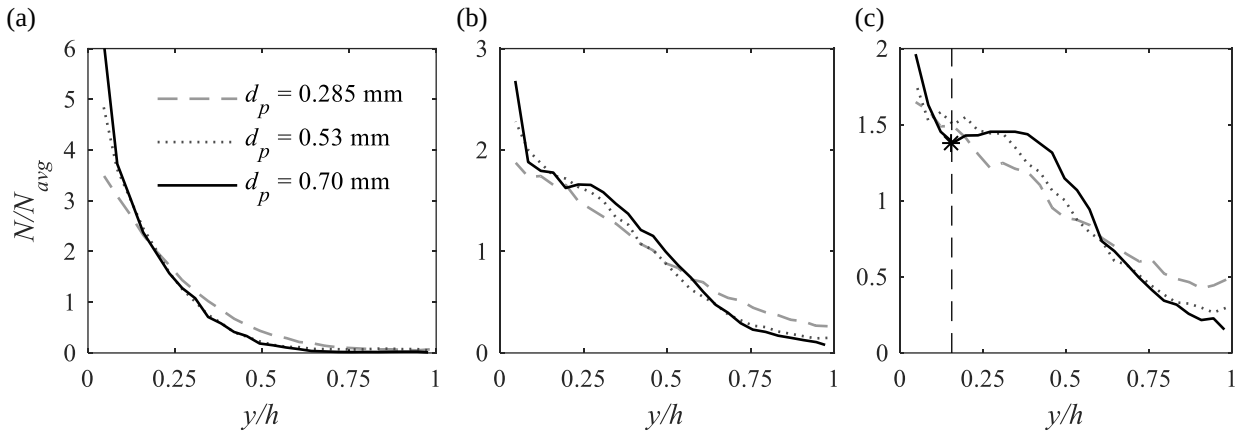

Fig. 14. The number density distribution for d_p = 285 μm, 530 μm, and 700 μm particles at (a) *Re* = 50,000, (b) *Re* = 100,000 and (c) *Re* = 125,000. The number of particles in each bin is divided by the average number of particles in the bins.

4.5. Effects of volumetric concentration on turbulence intensity

The influence of particle volumetric concentration on the mean velocity and turbulence intensity of the liquid and solid phases over the bottom half of the channel for d_p = 340 μm particles at *Re* = 125,000 is shown in Fig. 15 for φ_v = 0.03% to 0.18% (mass loading of 0.48%). At higher concentrations, the blockage of the line-of-sight of the cameras by the glass beads (i.e., occlusion) becomes significant. The 340 μm beads located between the channel sidewall and laser sheet block approximately 8%, 24%, and 48% of the image area at volumetric concentrations of 0.03%, 0.09% and 0.18%, respectively. These issues limit the current planar PIV/PTV measurement to 0.18% concentration.

Increasing φ_v from 0.03% to 0.18% has an insignificant effect on the solid and liquid phase mean velocity as indicated in Fig. 15a. It is also shown in Fig. 15b-d that increasing the volumetric concentration to 0.18% has only a slight impact on the turbulence intensities and Reynolds shear stress of the glass beads. Comparing the results with the literature shows that the negligible variation is due to the low volumetric concentration. Large eddy simulations of gas-solid flow in a downward channel conducted by Yamamoto et al. (2001) revealed that inter-particle collisions reduce $<u^2>$ and intensify $<v^2>$ of 70 μm copper particles at φ_v = 0.014%. Yamamoto et al. (2001) stated that the particle-particle collisions convert the energy in streamwise turbulent fluctuations to the wall-normal direction. The same trend is observed by Nouri et al. (1987) in a downward liquid-solid flow. The $<u^2>$ of particles decreased by about 20% as the volumetric concentration of 270 μm acrylic beads increased from 6% to 15%. Reduction in $<u^2>$ of the particulate phase with increasing particle concentration occurs at much lower volumetric concentrations in gas flows. Tsuji and Morikawa (1982) observed that the streamwise fluctuations of 200 μm particles decreased when the volumetric concentration was increased from 0.04% to 0.33% (mass loading changed from 0.4 to 3.3). The number of inter-particle collisions increases with the number of particles contained in the flow. Hence, the streamwise turbulence intensity should decrease, and

the wall-normal turbulence intensity of the solid phase should increase at higher volumetric concentrations. This implies that the collisions between particles is negligible over the range of concentrations investigated in the current study.

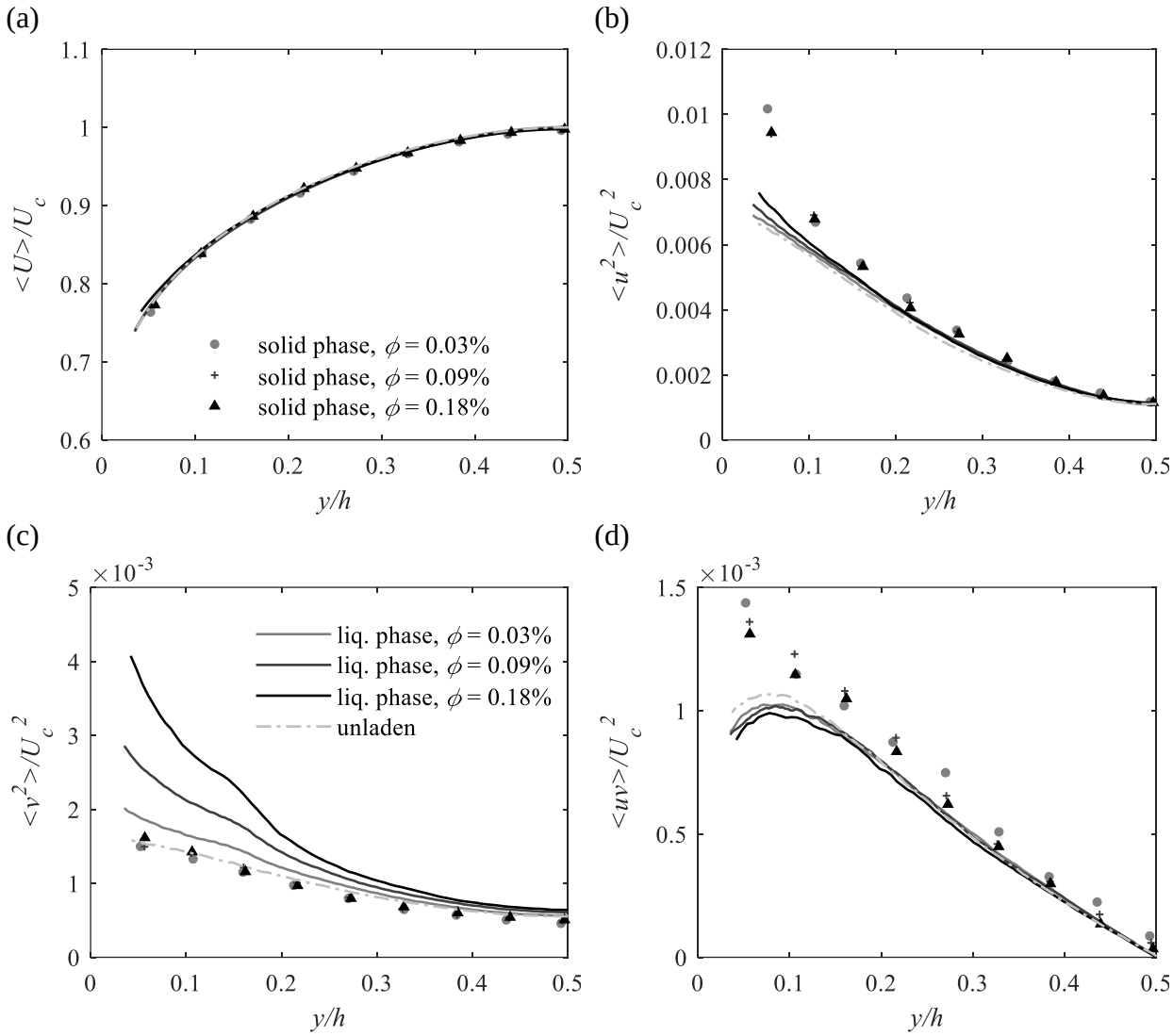

Fig. 15. The profiles of (a) mean streamwise velocity, (b) streamwise turbulence intensity, (c) wall-normal turbulence intensity, and (d) Reynolds shear stress at *Re* = 125,000. The statistics of the unladen flow is also shown with the dashed line for comparison.

Figures 15b and d show that varying the volumetric concentration of the solid phase has a negligible effect on $<u^2>$ and $<uv>$ of the liquid phase at $y/h > 0.1$. However, Fig. 15b indicates that $<v^2>$ of the liquid phase increases with the increase of volumetric concentration. The influence of particles on the liquid phase indicates that two-way coupling exists between the solid and liquid phases. The impact of volumetric concentration at *Re* = 75,000 is also similar to *Re* = 125,000 (as shown in Fig. 15); the results for *Re* = 75,000 are not presented here for brevity.

4.6. Turbulence modulation

The addition of solid particles to the flow can either increase or decrease carrier phase turbulence. The difference between the rms of streamwise velocity fluctuation of the liquid phase in the particle-laden and the unladen experiments measured at the channel centerline (y/h = 0.5) is defined as turbulence modulation, i.e.:

$$M(\%) = \frac{\sqrt{\langle u^2 \rangle_{PL}} - \sqrt{\langle u^2 \rangle_{UL}}}{\sqrt{\langle u^2 \rangle_{UL}}} \times 100, \quad (7)$$

where the subscript *PL* refers to the particle-laden and *UL* denotes the unladen flow. Several investigations have been carried out to predict *M* in particle-laden flows. Tanaka and Eaton (2008) suggest a dimensionless number called particle momentum number, *Pa*, to predict turbulence modulation of the particles. The *Pa* is defined as

$$Pa = \frac{1}{54\sqrt{2}} \frac{Re^2}{St^{0.5}} \frac{\rho_p^{1.5}}{\rho_f^{1.5}} \left(\frac{d_p}{h}\right)^3. \quad (8)$$

Tanaka and Eaton (2008) showed, using 80 data points, that turbulence modulation can be divided into three regions based on two critical *Pa* in the *Re* versus *Pa* plot as represented in Fig. 16. These two dimensionless numbers are selected since they appear in non-dimensional particle-laden Navier-Stokes equation. However, it appears that the classification mainly depends on *Pa*, and *Re* has little effect, at least in the studied range of *Re*, which is limited to 30,000. The critical particle momentum numbers are $Pa_{c1} \sim 10^3$ and $Pa_{c2} \sim 10^5$, and the turbulence is attenuated when $Pa_{c1} < Pa < Pa_{c2}$. The particles with $Pa > Pa_{c2}$ or $Pa < Pa_{c1}$ will augment the carrier phase turbulence. The previous data summarized by Tanaka and Eaton (2008), which includes turbulence modulation in air (indicated by circular markers) and also augmentation in the liquid phase (indicated by square symbols), are shown in Fig. 16a. In order to evaluate the established criterion at a higher range of *Re*, the cases from the current experiments that have a modulation larger than 2% have also been added to Fig 16a. These cases include the 700 μm particles at *Re* of 75,000, 100,000 and 125,000 at φ_v = 0.05% and also the 340 μm particles at *Re* = 125,000 and φ_v = 0.18%. The particle momentum number is close to Pa_{c1} for these four data points, and the liquid phase turbulence increases as predicted using the criterion of Tanaka and Eaton (2008). The variation of turbulence modulation with *Pa* for the aforementioned cases is depicted in Fig. 16b. These data points fall within the range of $620 < Pa < 1{,}200$. An increase in *M* with the increase in *Pa* is observed in this range, implying that turbulence augmentation in water can probably also occur at $Pa > 10^3$. The turbulence intensity of the liquid phase in two-phase flow is compared with the turbulence intensity of the solid phase at the channel centerline using the relative turbulence intensity (R_{TI}), defined as

$$R_{TI}(\%) = \frac{\sqrt{\langle u^2 \rangle_p} - \sqrt{\langle u^2 \rangle_l}}{\sqrt{\langle u^2 \rangle_l}} \times 100, \quad (9)$$

where the subscript *p* refers to the solid phase, and the *l* denotes the liquid phase. The results for the conditions shown in the first row of Table 1 are displayed in Fig. 17. A number of previous experiments were also examined, and the corresponding relative turbulence intensity was estimated. The results are also presented in Fig. 17. The collected experimental data includes gas-solid flow in a channel (Kulick et al., 1994; Laín et al., 2002; Wu et al., 2006) and pipe (Lee and Durst, 1982; Varaksin et al., 2000) in horizontal and vertical orientations. Gas flows result in larger *St* than liquid flows at any given *Re*. The data also contains experimental measurements in vertical liquid flow with ceramic, polystyrene (Alajbegović et al., 1994), and glass (Kameyama et al., 2014) beads. The details of these experiments are summarized in Table 4. The table highlights the lack of any measurement of turbulence intensity in a horizontal solid-liquid channel as addressed by the current investigation.

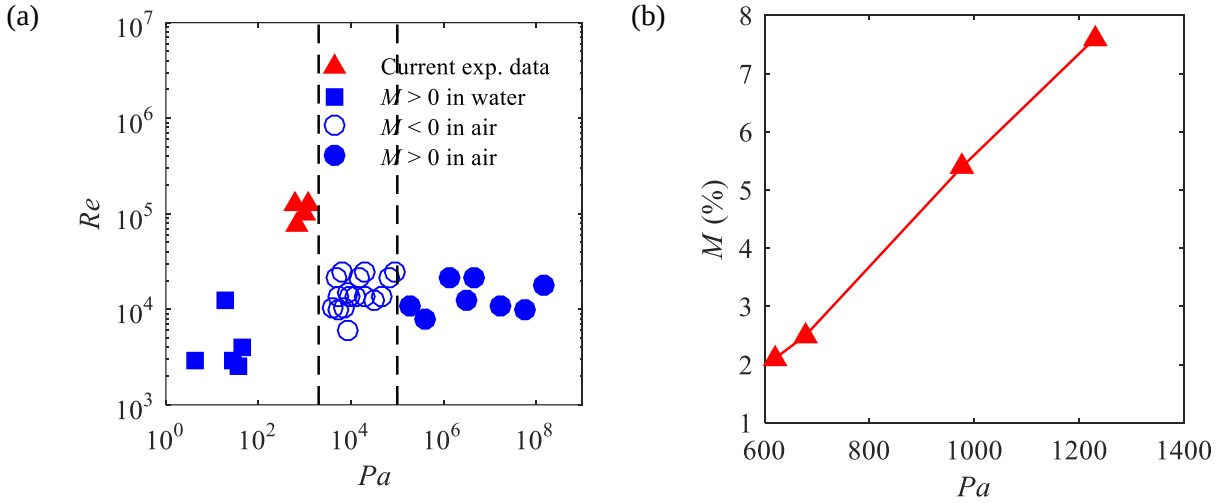

Fig. 16. (a) Mapping of the experimental data for turbulence modification. The data from the literature are collected by Tanaka and Eaton (2008), which include the turbulence augmentation and attenuation in air, and turbulence augmentation in water that are indicated in blue. The data of the current experiments which correspond to $Pa < Pa_{c1}$ region (augmentation in water) are presented in red. (b) Streamwise turbulence modulation for current experimental data as a function of *Pa*.

For very low *St* ($< 10^{-3}$) and low φ_v, the particles act as tracers. Hence, $R_{TI} \sim 0$ at very low *St*, and gradually increases until $St \sim 2$. In the *St* range of the current experiments ($4.1 < St < 40.6$), R_{TI} decreases with *St* as shown in Fig. 17. This is associated with the reduction of turbulence intensity of the particulate phase due to the decrease in transfer of turbulent kinetic energy to particles with larger *St*. When $St > 15$, $R_{TI} < 0$, indicating that the solid phase has smaller turbulence intensity relative to the liquid phase. The line fitted to the current experimental results for a horizontal solid-liquid flow shows that the relative turbulence intensity changes with the *St* as $R_{TI} = -14.0\ ln(St) + 38.5$.

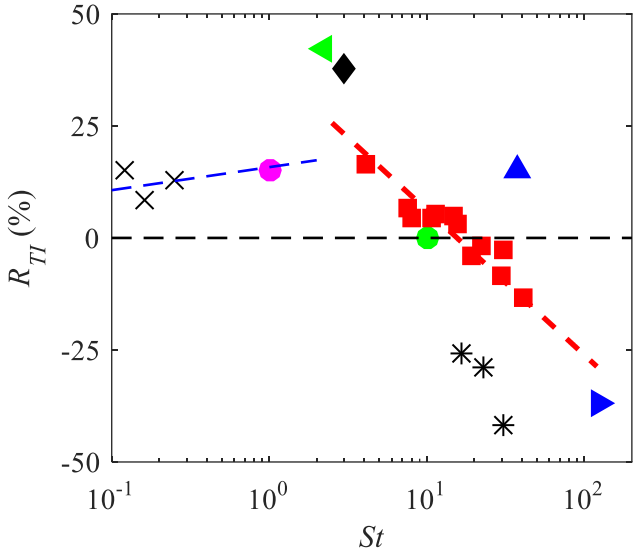

Fig. 17. The turbulence intensity of the solid phase relative to the liquid phase as defined in Eq. (9). The results of the current experiment (■) are fitted by R_{TI} = -14.0 $ln(St)$ + 38.5 (— —). The other symbols show the relative turbulence intensity obtained from Alajbegović et al. (1994) for polystyrene (×) and ceramic particles (*), Lee and Durst (1982) (►), Kulick et al. (1994) (●), Varaksin et al. (2000) (◄), Laín et al. (2002) (▲), Wu et al. (2006) (♦), and Kameyama et al. (2014) (●). The experimental conditions of these works are summarized in Table 4.

Table 4
Summary of previous experiments used to estimate the relative turbulence intensity (R_{TI}) of the solid and liquid phase.

Ref.	Flow descriptions	Carrier phase	Particles	*Re*
Alajbegović et al. (1994)	Upward pipe	Water	Ceramic	60-92 × 10^3
Alajbegović et al. (1994)	Upward pipe	Water	Polystyrene	60-92 × 10^3
Lee and Durst (1982)	Upward pipe	Air	Glass	15 × 10^3
Kulick et al. (1994)	Downward channel	Air	Glass	27.6 × 10^3
Varaksin et al. (2000)	Horizontal pipe	Air	Glass	15.3 × 10^3
Laín et al. (2002)	Horizontal channel	Air	Glass	36 × 10^3
Wu et al. (2006)	Horizontal channel	Air	Polythene	13.6 × 10^3
Kameyama et al. (2014)	Downward pipe	Water	Glass	19.5 × 10^3

5. Conclusions

The turbulence of both the solid and liquid phases for flow of two-phase mixtures in a horizontal channel has been investigated using PIV/PTV techniques. Flows with *Re* of 50,000, 75,000, 100,000 and 125,000 were investigated to study the effect of *Re* on turbulence statistics for different particle sizes. Glass beads of d_p = 285, 530, and 700 μm were used to investigate the effect of particle size at *Re* of 50,000 and 125,000. The effect of volumetric concentration of the particulate phase was also studied over the range $0.03\% \leq \varphi_v \leq 0.18\%$. The instantaneous velocity of the liquid phase was obtained using cross-correlation, and the solid phase velocity was measured by particle tracking from a common set of images.

The results demonstrated that smaller particles (d_p = 285 μm) are slower than the liquid phase at all *Re* tested, over the region $0.03 < y/h < 0.5$ where statistically reliable data for the particulate phase is available. Larger particles at higher *Re* lead the flow in the near-wall region while their velocity is lower than the liquid phase at $y/h > 0.3$. The mean streamwise velocity of the solid phase increased near the wall with increasing *St*. The crossing point, which shows the point where the particle and liquid velocities are equal, moves toward the channel centerline with increase of *St*.

In general, larger particles produced a greater increase in streamwise and wall-normal turbulence intensity of the carrier phase. In case of the largest particles (d_p = 700 μm), the liquid phase turbulence intensity was larger than the unladen flow, and the turbulence is augmented as *Re* increases. A maximum turbulence modulation of 7.6% was observed for d_p = 700 μm at *Re* = 125,000. This has been associated with the large particle Reynolds number ($Re_p \sim 250$) in the near-wall region, which is large enough to generate vortex shedding and enhance carrier phase turbulence. The measured turbulence modulation is shown to be reasonably well predicted using the criterion established by Tanaka and Eaton (2008).

The investigation of solid phase velocity fluctuation showed that the streamwise and wall-normal turbulence intensity of the solid phase decreased as the particle size and *Re* increased (i.e., with increasing *St*). Comparison with the literature reveals that there is a critical Stokes number (St_{cr}) which divides the variation of particle turbulence into two regimes. For $St < St_{cr}$, the turbulence intensity of the solid phase increases with *St* while it decreases for $St > St_{cr}$. The turbulence intensity of the solid phase is also compared to the liquid phase turbulence using R_{TI}, the relative turbulence intensity. The results show that R_{TI} varies with the *St* as $R_{TI} = -14.0\ ln(St) + 38.5$ for the *St* range of the current experimental study.

The particle number density distributions obtained here indicate that at relatively low *Re* and large particle size, when the particle terminal settling velocity is much larger than the friction velocity, the particle number density increases monotonically from the center of the channel towards the bottom wall. The distribution of particles becomes more uniform with increasing *Re*, since the turbulent dispersion force increases with increasing *Re*. A local minimum was observed in the

particle number density profile at $y/h \sim 0.15$ for the largest particles (d_p = 700 μm) at the highest *Re* tested here (*Re* = 125,000). This local minimum is associated with turbophoresis. The turbophoretic force pushes the particles toward the wall at $y/h < 0.15$ and toward the channel centerline at $y/h > 0.15$.

It was determined that varying the particle concentration from 0.03 to 0.18% had no significant effect on the solid phase turbulent statistics but does affect the liquid phase turbulence intensity, especially the wall-normal Reynolds stress. It is concluded that over this range of particle concentrations, there is no interaction between particles, and the liquid and solid phases interact through two-way coupling.

Appendix: PTV error analysis

The errors due to alignment of the laser sheet, deviation of the time delay between the laser pulses, and change in magnification across the field-of-view are negligible in the current PTV setup. The latter source is small since the observation angle is less than 3º and the working distance is larger than the field-of-view. The uncertainty in measurement of the channel height can also lead to error in calculating the scaling factor. This is estimated to be about $\varepsilon_M = 7.3\times10^{-5}$ mm/pix based on an assumed uncertainty of 0.1 pix. The main source of random error in PTV algorithm is due to overlapping particle images, low signal-to-noise ratio (SNR), and uncertainty in particle location (Kähler et al., 2012). The error associated with the overlapping particles is negligible here because of the small number of glass beads in the each image. The SNR is also enhanced by subtraction of the minimum value over an ensemble of images. In the current study, the PTV algorithm is followed by cross-correlation of two interrogation windows around the particle pair (as presented in Fig. 3). The cross-correlation reduces the uncertainty associated with the inaccurate estimation of glass beads position with a large non-Gaussian intensity. The remaining error in determining the displacement based on the cross-correlation with sub-pixel accuracy is about ε_{cc} = 0.1 pix (Westerweel et al., 1997). The root mean square (rms) uncertainty of the particle displacement $\varepsilon_{\Delta s}$ is given by

$$\varepsilon_{\Delta s} = \sqrt{(M\varepsilon_{cc})^2 + \left(\frac{\Delta s}{M}\varepsilon_M\right)^2}, \tag{10}$$

where M is digital resolution and Δs is the particle displacement between frames that varies from 12 pix near the wall to 20 pix at the channel centerline. The computed $\varepsilon_{\Delta s}$ is about 1.5×10^{-3} mm across the channel. The rms uncertainty of the instantaneous velocity ε_U is estimated using

$$\varepsilon_U = \sqrt{\left(\frac{1}{\Delta t}\varepsilon_{\Delta s}\right)^2 + \left(\frac{\Delta s}{\Delta t^2}\varepsilon_{\Delta t}\right)^2}. \tag{11}$$

The error in the mean velocity, velocity fluctuation, and turbulence intensity is calculated using the error propagation method. The normalized uncertainty at the middle of channel and also near the wall is reported in Table 5.

Table 5
Summary of rms measurement uncertainty estimated using error propagation method.

Parameter	y/h = 0.05	y/h = 0.25	y/h = 0.5
ε_U (mm/s)	28.8	30.7	32.7
$\varepsilon_{\langle U\rangle/U_c}$	4.7×10^{-5}	5.5×10^{-5}	7.8×10^{-5}
$\varepsilon_{\langle u^2\rangle/U_c^2}$	7.9×10^{-6}	7.1×10^{-6}	6.4×10^{-6}
$\varepsilon_{\langle v^2\rangle/U_c^2}$	3.8×10^{-6}	3.4×10^{-6}	4.3×10^{-6}
$\varepsilon_{\langle uv\rangle/U_c^2}$	4.4×10^{-6}	4.0×10^{-6}	3.9×10^{-6}

As an alternative method to estimate the random error is through statistical convergence of the $\langle U\rangle$, $\langle u^2\rangle$, $\langle v^2\rangle$ and $\langle uv\rangle$ of the solid phase at the channel centerline as shown in Fig. 18. The statistics reach a plateau after about 3,000 data points. The random error is also estimated using the difference between the maximum and minimum values in the last 3000 data points at three locations. The estimated errors are shown in Table 6 for comparison with the results of Table 5. It can be seen that the estimation based on statistical convergence results in larger uncertainty than the error propagation method.

Table 6
Estimation of random error at the channel centerline based on the convergence history of statistics.

Parameter	y/h = 0.05	y/h = 0.25	y/h = 0.5
$\varepsilon_{\langle U\rangle/U_c}$	6.1×10^{-4}	4.3×10^{-4}	1.1×10^{-3}
$\varepsilon_{\langle u^2\rangle/U_c^2}$	1.2×10^{-4}	2.9×10^{-5}	4.9×10^{-5}
$\varepsilon_{\langle v^2\rangle/U_c^2}$	6.4×10^{-5}	2.1×10^{-5}	1.4×10^{-5}
$\varepsilon_{\langle uv\rangle/U_c^2}$	2.5×10^{-5}	1.8×10^{-5}	1.6×10^{-5}

(a) (b)

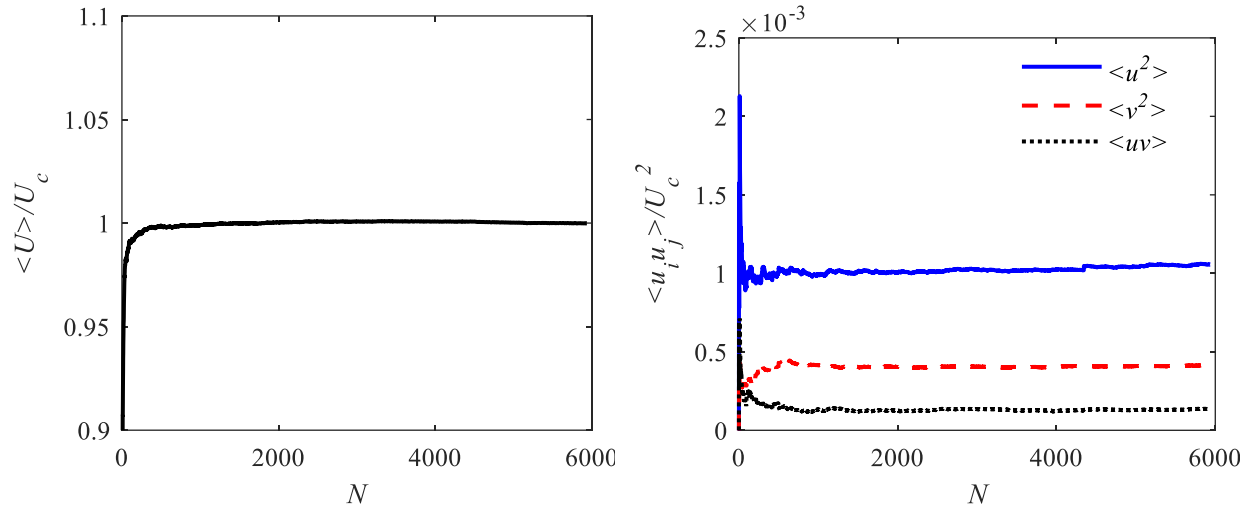

Fig. 18. The convergence of (a) mean velocity, (b) Reynolds stresses of the solid phase at the channel centerline for flow with d_p = 530 μm particles at *Re* of 100,000.

References

Alajbegović, A., Assad, A., Bonetto, F., Lahey, R.T., 1994. Phase distribution and turbulence structure for solid/fluid upflow in a pipe. Int. J. Multiph. Flow 20, 453–479. doi:10.1016/0301-9322(94)90021-3

Anderson, S.L., Longmire, E.K., 1996. Interpretation of PIV autocorrelation mesurements in complex particle-laden flows. Exp. Fluids 20, 314–317. doi:10.1007/BF00192676

Atherton, T.J., Kerbyson, D.J., 1999. Size invariant circle detection. Image Vis. Comput. 17, 795–803. doi:10.1016/S0262-8856(98)00160-7

Balachandar, S., Eaton, J.K., 2010. Turbulent Dispersed Multiphase Flow. Annu. Rev. Fluid Mech. 42, 111–133. doi:10.1146/annurev.fluid.010908.165243

Brenn, G., Braeske, H., Živković, G., Durst, F., 2003. Experimental and numerical investigation of liquid channel flows with dispersed gas and solid particles. Int. J. Multiph. Flow 29, 219–247. doi:10.1016/S0301-9322(02)00133-7

Caporaloni, M., Tampieri, F., Trombetti, F., Vittori, O., 1975. Transfer of Particles in Nonisotropic Air Turbulence. J. Atmos. Sci. 32, 565–568. doi:10.1175/1520-0469(1975)032<0565:TOPINA>2.0.CO;2

Clauser, F.H., 1956. The Turbulent Boundary Layer. Adv. Appl. Mech. 4, 1–51. doi:10.1016/S0065-2156(08)70370-3

Delnoij, E., Westerweel, J., Deen, N.G., Kuipers, J.A.M., van Swaaij, W.P.M., 1999. Ensemble correlation PIV applied to bubble plumes rising in a bubble column. Chem. Eng. Sci. 54, 5159–5171. doi:10.1016/S0009-2509(99)00233-X

Doroodchi, E., Evans, G.M., Schwarz, M.P., Lane, G.L., Shah, N., Nguyen, A., 2008. Influence

of turbulence intensity on particle drag coefficients. Chem. Eng. J. 135, 129–134. doi:10.1016/J.CEJ.2007.03.026

Gore, R.A., Crowe, C.T., 1989. Effect of particle size on modulating turbulent intensity. Int. J. Multiph. Flow 15, 279–285. doi:10.1016/0301-9322(89)90076-1

Hassan, Y.A., Blanchat, T.K., Seeley, C.H., Canaan, R.E., 1992. Simultaneous velocity measurements of both components of a two-phase flow using particle image velocimetry. Int. J. Multiph. Flow 18, 371–395. doi:http://dx.doi.org/10.1016/0301-9322(92)90023-A

Hout, R. van, 2011. Time-resolved PIV measurements of the interaction of polystyrene beads with near-wall-coherent structures in a turbulent channel flow. Int. J. Multiph. Flow 37, 346–357. doi:10.1016/J.IJMULTIPHASEFLOW.2010.11.004

Kähler, C.J., Scharnowski, S., Cierpka, C., 2012. On the uncertainty of digital PIV and PTV near walls. Exp. Fluids 52, 1641–1656. doi:10.1007/s00348-012-1307-3

Kameyama, K., Kanai, H., Kawashima, H., Ishima, T., 2014. Evaluation of particle motion in solid-liquid two-phase pipe flow with downward/upward flow directions. 17th Internatonal Symp. Appl. Laser Tech. to Fluid Mech. 1–15.

Khalitov, D.A., Longmire, E.K., 2002. Simultaneous two-phase PIV by two-parameter phase discrimination. Exp. Fluids 32, 252–268. doi:10.1007/s003480100356

Kiger, K.T., Pan, C., 2002. Suspension and turbulence modification effects of solid particulates on a horizontal turbulent channel flow. J. Turbul. 3, N19. doi:10.1088/1468-5248/3/1/019

Kiger, K.T., Pan, C., 2000. PIV technique for the simultaneous measurement of dilute two-phase flows. Trans. Soc. Mech. Eng. J. FLUIDS Eng. 122, 811–818.

Kulick, J.D., Fessler, J.R., Eaton, J.K., 1994. Particle response and turbulence modification in fully developed channel flow. J. Fluid Mech. 277, 109. doi:10.1017/S0022112094002703

Kussin, J., Sommerfeld, M., 2002. Experimental studies on particle behaviour and turbulence modification in horizontal channel flow with different wall roughness. Exp. Fluids 33, 143–159. doi:10.1007/s00348-002-0485-9

Laín, S., Sommerfeld, M., Kussin, J., 2002. Experimental studies and modelling of four-way coupling in particle-laden horizontal channel flow. Int. J. Heat Fluid Flow 23, 647–656. doi:10.1016/S0142-727X(02)00160-1

Lee, J.H., Kevin, Monty, J.P., Hutchins, N., 2016. Validating under-resolved turbulence intensities for PIV experiments in canonical wall-bounded turbulence. Exp. Fluids 57, 129. doi:10.1007/s00348-016-2209-6

Lee, S.L., 1987. Particle drag in a dilute turbulent two-phase suspension flow. Int. J. Multiph. Flow 13, 247–256. doi:10.1016/0301-9322(87)90032-2

Lee, S.L., Durst, F., 1982. On the motion of particles in turbulent duct flows. Int. J. Multiph. Flow 8, 125–146. doi:10.1016/0301-9322(82)90013-1

Li, D., Wei, A., Kun, L., Jianren, F., 2016. Direct numerical simulation of a particle-laden flow in a flat plate boundary layer. Int. J. Multiph. Flow 79, 124–143. doi:10.1016/J.IJMULTIPHASEFLOW.2015.10.011

Li, Y., McLaughlin, J.B., Kontomaris, K., Portela, L., 2001. Numerical simulation of particle-laden turbulent channel flow. Phys. Fluids 13, 2957–2967. doi:10.1063/1.1396846

Marchioli, C., Giusti, A., Salvetti, M.V., Soldati, A., 2003. Direct numerical simulation of particle wall transfer and deposition in upward turbulent pipe flow. Int. J. Multiph. Flow 29, 1017–1038. doi:10.1016/S0301-9322(03)00036-3

Marchioli, C., Soldati, A., 2002. Mechanisms for particle transfer and segregation in a turbulent boundary layer. J. Fluid Mech. 468, 283–315. doi:DOI: 10.1017/S0022112002001738

Meinhart, C.D., Wereley, S.T., Santiago, J.G., 2000. A PIV algorithm for estimating time-averaged velocity fields. J. Fluids Eng. 122, 285–289.

Milojević, D., 1990. Lagrangian Stochastic-Deterministic (LSD) Predictions of Particle Dispersion in Turbulence. Part. Part. Syst. Charact. 7, 181–190. doi:10.1002/ppsc.19900070132

Moser, R.D., Kim, J., Mansour, N.N., 1999. Direct numerical simulation of turbulent channel flow up to Reτ=590. Phys. Fluids 11, 943–945. doi:10.1063/1.869966

Nouri, J.M., Whitelaw, J.H., Yianneskis, M., 1987. Particle motion and turbulence in dense two-phase flows. Int. J. Multiph. Flow 13, 729–739. doi:10.1016/0301-9322(87)90062-0

Picano, F., Breugem, W.-P., Brandt, L., 2015. Turbulent channel flow of dense suspensions of neutrally buoyant spheres. J. Fluid Mech. 764, 463–487. doi:10.1017/jfm.2014.704

Pope, S.B., 2000. Turbulent Flows. Cambridge University Press, Cambridge. doi:10.1017/CBO9780511840531

Raffel, M., Willert, C.E., Kompenhans, J., others, 2007. Particle image velocimetry: a practical guide. Springer Science & Business Media.

Rashidi, M., Hetsroni, G., Banerjee, S., 1990. Particle-turbulence interaction in a boundary layer. Int. J. Multiph. Flow 16, 935–949. doi:10.1016/0301-9322(90)90099-5

Reeks, M.W., 1983. The transport of discrete particles in inhomogeneous turbulence. J. Aerosol Sci. 14, 729–739. doi:10.1016/0021-8502(83)90055-1

Righetti, M., Romano, G.P., 2004. Particle–fluid interactions in a plane near-wall turbulent flow. J. Fluid Mech. 505, 93–121. doi:DOI: 10.1017/S0022112004008304

Roco, M.C., Addie, G.R., 1987. Erosion wear in slurry pumps and pipes. Powder Technol. 50, 35–46. doi:10.1016/0032-5910(87)80081-5

Saffman, P.G., 1965. The lift on a small sphere in a slow shear flow. J. Fluid Mech. 22, 385–400. doi:DOI: 10.1017/S0022112065000824

Schlichting, H., Gersten, K., 2017. Boundary-Layer Theory. Springer, Berlin, Heidelberg. doi:https://doi.org/10.1007/978-3-662-52919-5

Shokri, R., Ghaemi, S., Nobes, D.S., Sanders, R.S., 2017. Investigation of particle-laden turbulent pipe flow at high-Reynolds-number using particle image/tracking velocimetry (PIV/PTV). Int. J. Multiph. Flow 89, 136–149. doi:10.1016/j.ijmultiphaseflow.2016.06.023

Shook, C.A., McKibben, M., Small, M., 1990. Experimental investigation of some hydrodynamic factors affecting slurry pipeline wall erosion. Can. J. Chem. Eng. 68, 17–23. doi:10.1002/cjce.5450680102

Sommerfeld, M., 2003. Analysis of collision effects for turbulent gas–particle flow in a horizontal channel: Part I. Particle transport. Int. J. Multiph. Flow 29, 675–699. doi:10.1016/S0301-9322(03)00031-4

Sridhar, G., Katz, J., 1995. Drag and lift forces on microscopic bubbles entrained by a vortex. Phys. Fluids 7, 389–399. doi:10.1063/1.868637

Sumer, B.M., Oguz, B., 1978. Particle motions near the bottom in turbulent flow in an open channel. J. Fluid Mech. 86, 109. doi:10.1017/S0022112078001020

Tanaka, T., Eaton, J.K., 2008. Classification of turbulence modification by dispersed spheres using a novel dimensionless number. Phys. Rev. Lett. 101, 1–4. doi:10.1103/PhysRevLett.101.114502

Taneda, S., 1956. Experimental Investigation of the Wake behind a Sphere at Low Reynolds Numbers. J. Phys. Soc. Japan 11, 1104–1108. doi:10.1143/JPSJ.11.1104

Tennekes, H., Lumley, J.L., 1972. A First Course in Turbulence. MIT Press.

Tsuji, Y., Morikawa, Y., 1982. LDV measurements of an air–solid two-phase flow in a horizontal pipe. J. Fluid Mech. 120, 385. doi:10.1017/S002211208200281X

Tsuji, Y., Morikawa, Y., Fujiwara, Y., 1985. Pipe flow with solid particles fixed in space. Int. J. Multiph. Flow 11, 177–188. doi:10.1016/0301-9322(85)90044-8

Tsuji, Y., Morikawa, Y., Shiomi, H., 1984. LDV measurements of an air-solid two-phase flow in a vertical pipe. J. Fluid Mech. 139, 417. doi:10.1017/S0022112084000422

Varaksin, A.Y., Polezhaev, Y.V., Polyakov, A.F., 2000. Effect of particle concentration on fluctuating velocity of the disperse phase for turbulent pipe flow. Int. J. Heat Fluid Flow 21, 562–567. doi:10.1016/S0142-727X(00)00045-X

Vreman, A.W., 2015. Turbulence attenuation in particle-laden flow in smooth and rough channels. J. Fluid Mech. 773, 103–136. doi:10.1017/jfm.2015.208

Westerweel, J., Dabiri, D., Gharib, M., 1997. The effect of a discrete window offset on the accuracy of cross-correlation analysis of digital PIV recordings. Exp. Fluids 23, 20–28. doi:10.1007/s003480050082

Wu, Y., Wang, H., Liu, Z., Li, J., Zhang, L., Zheng, C., 2006. Experimental investigation on

turbulence modification in a horizontal channel flow at relatively low mass loading. Acta Mech. Sin. 22, 99–108. doi:10.1007/s10409-006-0103-9

Yamamoto, Y., Potthoff, M., Tanaka, T., Kajishima, T., Tsuji, Y., 2001. Large-eddy simulation of turbulent gas–particle flow in a vertical channel: effect of considering inter-particle collisions. J. Fluid Mech. 442, 303–334. doi:DOI: 10.1017/S0022112001005092

Zhao, F., George, W., Van Wachem, B., 2015. Four-way coupled simulations of small particles in turbulent channel flow: The effects of particle shape and Stokes number. Phys. Fluids 27, 83301. doi:10.1063/1.4927277

Zisselmar, R., Molerus, O., 1979. Investigation of solid—liquid pipe flow with regard to turbulence modification. Chem. Eng. J. 18, 233–239. doi:10.1016/0300-9467(79)80123-9